frontiers | Frontiers in Earth Science

TYPE Original Research
PUBLISHED 19 March 2025
DOI 10.3389/feart.2025.1562893

OPEN ACCESS

EDITED BY
Zhongliang Wang,
China University of Geosciences, China

REVIEWED BY
Liang Qiu,
China University of Geosciences, China
Dapeng Li,
China University of Geosciences, China

*CORRESPONDENCE
Dechao Li,
175148361@qq.com
Xijun Liu,
xijunliu@glut.edu.cn

RECEIVED 18 January 2025
ACCEPTED 26 February 2025
PUBLISHED 19 March 2025

CITATION
Chen G, Li D, Liu X, Liu P, Bai Z, Liu X, Hu R, Tian H, Liu Y, Huang W and Xiao Y (2025) Petrogenesis of Middle Silurian Shandan diorites in North Qilian Orogenic Belt, NW China: Insights into post-collisional slab breakoff.
Front. Earth Sci. 13:1562893.
doi: 10.3389/feart.2025.1562893

Petrogenesis of Middle Silurian Shandan diorites in North Qilian Orogenic Belt, NW China: Insights into post-collisional slab breakoff

Gang Chen[1], Dechao Li[1,2]*, Xijun Liu[1,2,3]*, Pengde Liu[3], Zhihan Bai[1], Xiao Liu[1,2], Rongguo Hu[1,2], Hao Tian[1], Yande Liu[1], Wenmin Huang[1] and Yao Xiao[1]

[1]Guangxi Key Laboratory of Hidden Metallic Ore Deposits Exploration, College of Earth Sciences, Guilin University of Technology, Guilin, China, [2]Collaborative Innovation Center for Exploration of Nonferrous Metal Deposits and Efficient Utilization of Resources in Guangxi, Guilin University of Technology, Guilin, China, [3]National Key Laboratory of Arid Area Ecological Security and Sustainable Development, Xinjiang Institute of Ecology and Geography, Chinese Academy of Sciences, Urumqi, China

Paleozoic intrusive rocks are exposed in the Longshoushan area in NW China, in the Northern Qilian Block and on the southern edge of the Alxa Block. Understanding the petrogenesis and tectonic setting of these intrusive rocks is crucial for reconstructing the tectonic evolution and tectonomagmatic processes that occurred along the North Qilian Orogenic Belt between the Alxa and Central Qilian blocks. This study presents an integrated analysis of petrology, zircon U-Pb geochronology, whole-rock geochemistry, along with Sr–Nd–Pb isotopic data and zircon Hf–O isotopic analyses for these intrusive rocks. The Shandan intrusive rocks consist primarily of calc-alkaline quartz diorite (~430 Ma) and diorite (~403 Ma). These diorites are enriched in large-ion lithophile elements (e.g., Ba and U) and depleted in high field strength elements (e.g., Nb, Ta, and Ti), similar to subduction-related magmas. The Shandan diorites have enriched Sr and Nd isotopic compositions, with high initial $^{87}Sr/^{86}Sr$ ratios (0.705247–0.70618), variable $\varepsilon_{Nd}(t)$ values (–1.58 to –3.53), positive zircon $\varepsilon_{Hf}(t)$ values (+0.08 to +3.55) and low zircon $\delta^{18}O$ values (5.75‰–6.38‰). The older zircon grains (430 Ma) yield $\varepsilon_{Hf}(t)$ values of +0.14 to +6.58 and the younger grains (403 Ma) yield negative $\varepsilon_{Hf}(t)$ values (+2.24 to –11.0). The geochemical and isotopic data suggest that the diorites were derived through low-degree partial melting of enriched subcontinental lithospheric mantle with the addition of crustal material and subduction-related sediment-derived melts. We suggest that the formation of the Shandan diorites was dominated by slab breakoff at ~430 Ma, which created a window that enabled the upwelling of asthenospheric material and induced partial melting of the subcontinental lithospheric mantle and crust. At ~403 Ma, slab breakoff was nearing end, leading to weaker asthenospheric upwelling.

KEYWORDS

slab breakoff, Sr-Nd-Pb isotopic compositions, zircon Hf-O isotopic compositions, Shandan diorites, Longshoushan area

1 Introduction

Post-collisional magmatism offers insights into orogenic tectonics, magma evolution, and crust–mantle interactions (Jahn et al., 1999; Liégeois, 1998). These processes are important in regional reconstructions and shed light on the mechanisms applicable to similar orogenic settings worldwide (Zhang et al., 2023). The post-collisional phase represents a transition from crustal thickening to thinning, attributed to gravitational collapse or extension of the lithosphere (Liégeois, 1998; Vanderhaeghe and Teyssier, 2001). This sequence typically includes slab breakoff, lithospheric delamination, and convective thinning due to thickening of the lithospheric mantle (e.g., Bird, 1979; Houseman et al., 1981; Kay and Mahlburg Kay, 1993; Molnar et al., 1998; von Blanckenburg and Davies, 1995). Slab breakoff typically occurs ~1–5 Myr after continental collision due to density contrasts between the subducting oceanic and overriding continental lithospheres (Huw Davies and von Blanckenburg, 1995; von Blanckenburg and Davies, 1995). Slab breakoff induces convective upwelling in the asthenosphere, resulting in conductive heating that leads to the melting of the overlying mantle lithosphere. In turn, this results in the generation of basaltic and intermediate magmas, leading to granitic magmatism in the crust (van Hunen and Miller, 2015). The petrogenesis of post-collisional magmatic rocks, therefore, serves as a direct probe into the timing, triggers, and geodynamic consequences of slab breakoff, offering a window into deep lithospheric processes.

The North Qilian Orogenic Belt (NQOB), located between the Alxa and Central Qilian–Qaidam blocks in northeastern Tibet, is a typical Phanerozoic accretionary-to-collisional orogenic belt (Fu et al., 2020; Figure 1a). Numerous ophiolites, high-pressure/low-temperature metamorphic rocks, arc-related volcanic and intrusive suites, and flysch formations in the NQOB record the history of the North Qilian Ocean from seafloor spreading to subduction and closure (Song et al., 2013). Volcanic arc granitoids in the NQOB formed between 520 and 460 Ma and consist of diorite, granodiorite (Song et al., 2013; Wu et al., 2011), and S-type granite (Chen et al., 2014). The southern and northern margins of the Alxa Block are separated from the Central Asian and Qilian orogenic belts by the Badanjilin and Longshoushan faults, respectively. The extensive Paleozoic magmatic rocks in the Alxa Block provide an opportunity to study the tectonic evolution of the Paleo-Asian and Qilian oceans. Abundant Paleozoic volcanic rocks with crystallization ages of 460–230 Ma are exposed in the Alxa Block (Liu et al., 2016; Zeng et al., 2016).

The Longshoushan Belt, which is situated on the southern margin of the Alxa Block and the northern margin of the NQOB (Figure 1b), hosts abundant early Paleozoic intermediate to felsic igneous rocks (Zhang L. Q. et al., 2017). The early Paleozoic magmatic activity is thought to have been associated with northward subduction of the Northern Qilian oceanic crust followed by collision and post-collisional activity (Song et al., 2013; Zhang L. Q. et al., 2017). Previous investigations into the 445–403 Ma magmatic rocks in the Northern Qilian region suggest that they were emplaced in a post-collisional setting after closure of the Paleozoic Northern Qilian Ocean (Cao and Song, 2009; Song et al., 2013; Wang et al., 2005; Xu et al., 2010); however, the post-collisional evolution of the Longshoushan Belt during the Paleozoic is poorly constrained. The uncertainty is centered on the petrogenesis of the 444–400 Ma arc granitoids of the Longshoushan Belt (Duan et al., 2015; Wang et al., 2019; Zhang et al., 2019). The 444–400 Ma intermediate to felsic igneous rocks in the Longshoushan Belt are thought to have originated from partial melting of the Precambrian Longshoushan Group with limited input of mantle material (Zhao et al., 2016; Zhou et al., 2016) or through the mixing of re-melted felsic igneous rocks and mantle-derived magmas (Wang et al., 2019; Zhang et al., 2018). A fundamental enigma persists: discerning the precise geodynamic mechanisms driving this magmatism, particularly the transition from collisional to post-collisional extension. The Middle Silurian Shandan diorites, exposed along the North Qilian Orogenic Belt (NQOB) and the southern margin of the Alxa Block, represent a crucial, yet hitherto under-examined, component of this post-collisional magmatic suite. Their emplacement age, spanning approximately 430 to 420 Ma, coincides with the inferred timing of slab breakoff following the closure of the North Qilian Ocean (Song et al., 2013; Wang et al., 2005). These diorites display geochemical characteristics consistent with significant mantle-crust interaction, rendering them an ideal lithological unit for investigating the intricate interplay between slab breakoff, mantle dynamics, and crustal anatexis. However, the unresolved questions surrounding their petrogenesis, source regions, and broader tectonic significance currently hinder a comprehensive understanding of the post-collisional evolutionary trajectory of the NQOB.

This study presents zircon U–Pb geochronology, Hf–O isotopes, whole-rock geochemistry, and Sr–Nd–Pb isotopic data from the Shandan diorites. We aim to (1) constrain their emplacement age and elucidate their petrogenetic processes, (2) identify mantle and crustal contributions to their source, and (3) evaluate their implications for post-collisional slab breakoff dynamics. By addressing these fundamental questions, we seek to illuminate the role of slab breakoff in driving Silurian magmatism and lithospheric reworking within the NQOB, thereby providing new constraints on the transition from collisional thickening to post-collisional extensional tectonics in the North Qilian orogen.

2 Geological setting

The Alxa Block is a triangular-shaped terrane adjacent to the northern part of the NQOB, bounded by the North China Craton to the east, the Central Asian Orogenic Belt to the north, the Tarim Craton to the west, and the Qilian Block to the south (Zhang L. Q. et al., 2017; Figure 1). The northwest-trending Longshoushan Belt is 30 km wide and extends for ~300 km along the southwestern margin of the Alxa Block. It is bounded to the south by the dextral northwest-to west-striking Longshoushan Fault, which was active during the early Paleozoic Qilian Orogeny (Song et al., 2013; Zhang L. Q. et al., 2017). Large Palaeozoic granitic plutons occur along the boundary between the North Qilian Suture Zone and the Longshoushan Belt. Igneous rocks, ranging from ultrabasic dunite to granite, are abundant in the Longshoushan region (Gong et al., 2013; Liu et al., 2020). The sedimentary sequence above the Paleoproterozoic Longshoushan Group ranges from Mesoproterozoic to Paleozoic in age, beginning with the Mesoproterozoic Dunzigou Group, which unconformably overlies the basement rocks and consists mainly of low-grade metamorphic siliciclastic and carbonate formations

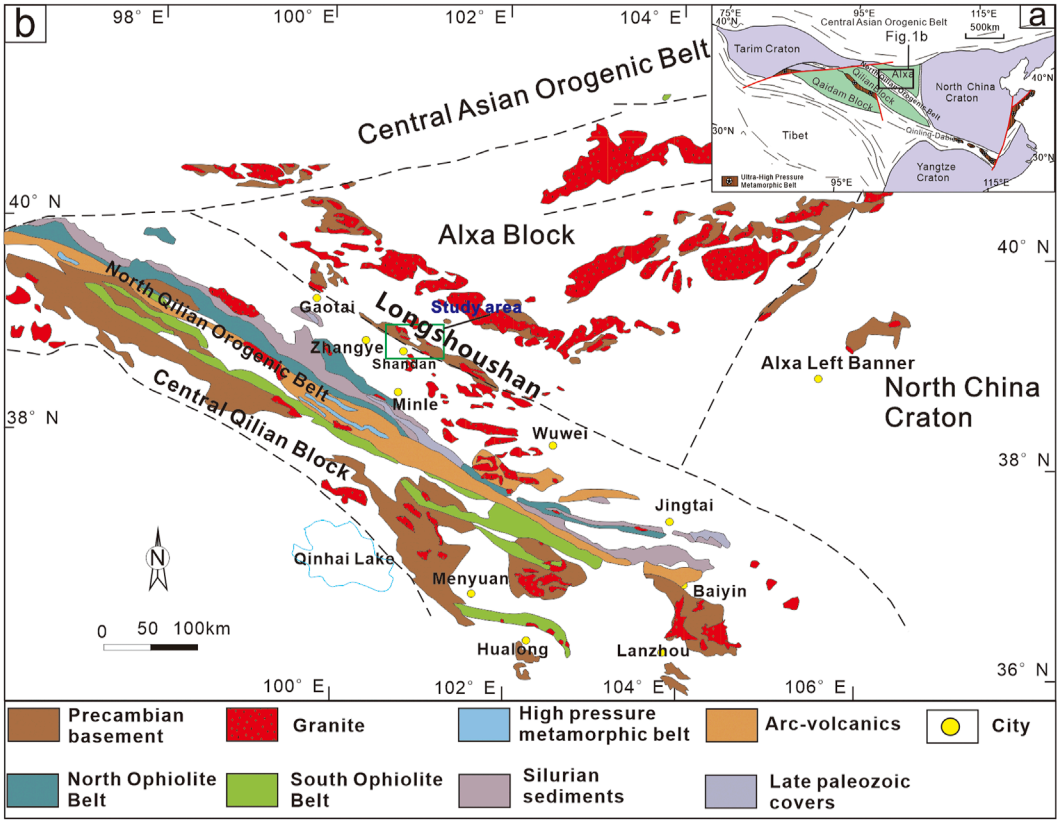

FIGURE 1
(a) Major tectonic units in China. **(b)** Geological map showing the distribution of magmatic rocks in the Qilian Orogenic Belt and Alxa Block (after Song et al., 2013; Zhang L. Q. et al., 2017).

(e.g., Gong et al., 2016; Wu et al., 2021). The Dunzigou Group is overlain by the Neoproterozoic Hanmushan Group (e.g., Gong et al., 2013), which contains rift-related siliciclastic rocks, limestone, mafic volcanic rocks, and glacial deposits. The Hanmushan Group is overlain by Cambrian strata, which are mostly exposed to the south of the Shandan Complex and consist of quartz sandstone, slate, and volcanic rocks intruded by late Paleozoic granitoids (e.g., Liu et al., 2020; Xue et al., 2017; Figure 2).

During the Paleozoic, the Longshoushan region was influenced mainly by the North Qilian Ocean tectonic regime to the south. The NQOB, also referred to as the North Qilian Accretionary Belt, is an elongate NW–SE-trending belt that extends for >1,000 km between the Alxa Block to the north and the Qilian Block to the south (Song et al., 2017; Zhang J. X. et al., 2017). The NQOB consists of two ophiolite belts, volcanic rocks, granitoids, high-pressure metamorphic rocks, and accretionary complexes, and provides an important record of the geological processes that occurred at an ancient convergent plate margin (Song et al., 2014; Song et al., 2013; Song et al., 2007; Wang et al., 2005; Wei and Song, 2008; Wei et al., 2009; Wu et al., 1993; Zhang J. X. et al., 2017; Zhang L. Q. et al., 2017). A Cambrian–Ordovician arc complex (~516–446 Ma), located between the two ophiolite belts, consists of boninitic complexes, felsic calc-alkaline volcanic rocks, and granitoid plutons (Song et al., 2013; Wang et al., 2005; Wu et al., 2010; Xia et al., 2003; Xia et al., 2012).

The Shandan Complex, which is located in the eastern segment of the northern margin of the NQOB (Figure 1b), consists primarily of ultramafic and mafic rocks, along with accretionary complexes containing serpentinized harzburgite, gabbro, basalt, and siliceous–argillaceous rocks. Extensive Paleozoic intrusive and volcanic rocks crop out in this area (Figures 2, 3). These rocks were emplaced sporadically during the Caledonian orogeny and are composed of quartz syenite, diorite, granodiorite, granite-diorite porphyrite dikes, and mafic dikes. The Shandan diorite is located at the southeastern part of the Shandan complex (Figure 3), intruding into the Cambrian Hanmushan Group's limestone, schist and tuff, with an intrusive contact relationship with both granite and granodiorite. The contact zone between the Shandan diorite body and the surrounding rocks exhibits well-developed schistosity and is distributed along N-W regional fault zones.

3 Sample description and analytical methods

3.1 Samples

Abundant magmatic rocks are exposed in the Shandan area to the west of the Longshoushan Fault. We collected several fresh samples of diorite and quartz diorite from the Shandan area.

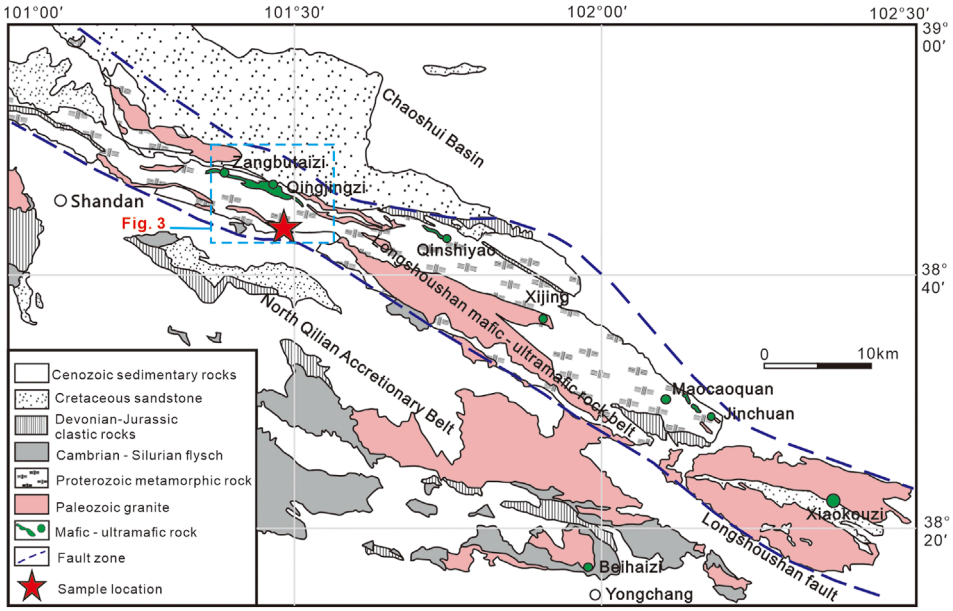

FIGURE 2
Simplified geological map of the Longshoushan region (modified after Duan et al., 2015).

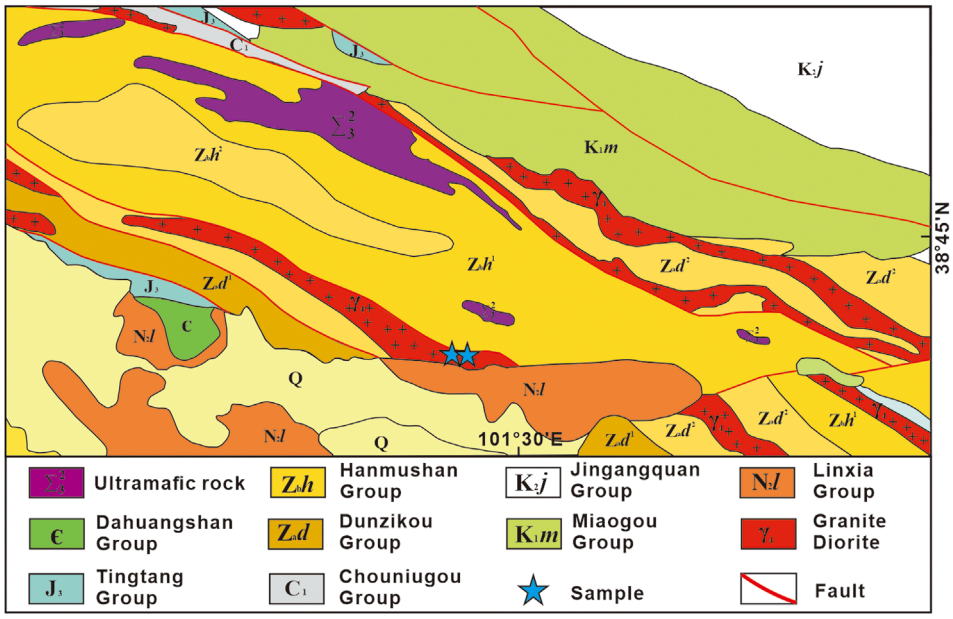

FIGURE 3
Geological map of the Shandan area, showing the distribution of Shandan Complex and sample locations.

These rocks are part of the Neoproterozoic Hanmushan Formation, which has been fractured and exposed due to subsequent tectonic movements. The sample locations are shown in Figures 2, 3.

The quartz diorite samples are fine-to medium-grained and consist mainly of plagioclase (40–45 vol%), amphibole (30–40 vol%), pyroxene (8–10 vol%), quartz (5–8 vol%), and titanite (2–4 vol%) (Figures 4a, 5a, b). Most crystals are euhedral to subhedral. Plagioclase occurs as subhedral laths 0.1–5.0 mm in length. Amphibole occurs as anhedral to subhedral crystals located between plagioclase crystals and is 0.1–1.5 mm in length.

The diorite is light to dark grey and medium-grained. It has a granular texture and is composed of plagioclase (55 vol%), amphibole (15–20 vol%), clinopyroxene (10–15 vol%), and magnetite (Figures 4b-d). Plagioclase grains are generally subhedral to anhedral and 0.3–1.0 mm in length. Anhedral to subhedral clinopyroxene (0.2–0.5 mm) and hornblende (0.25–3.0 mm) occur

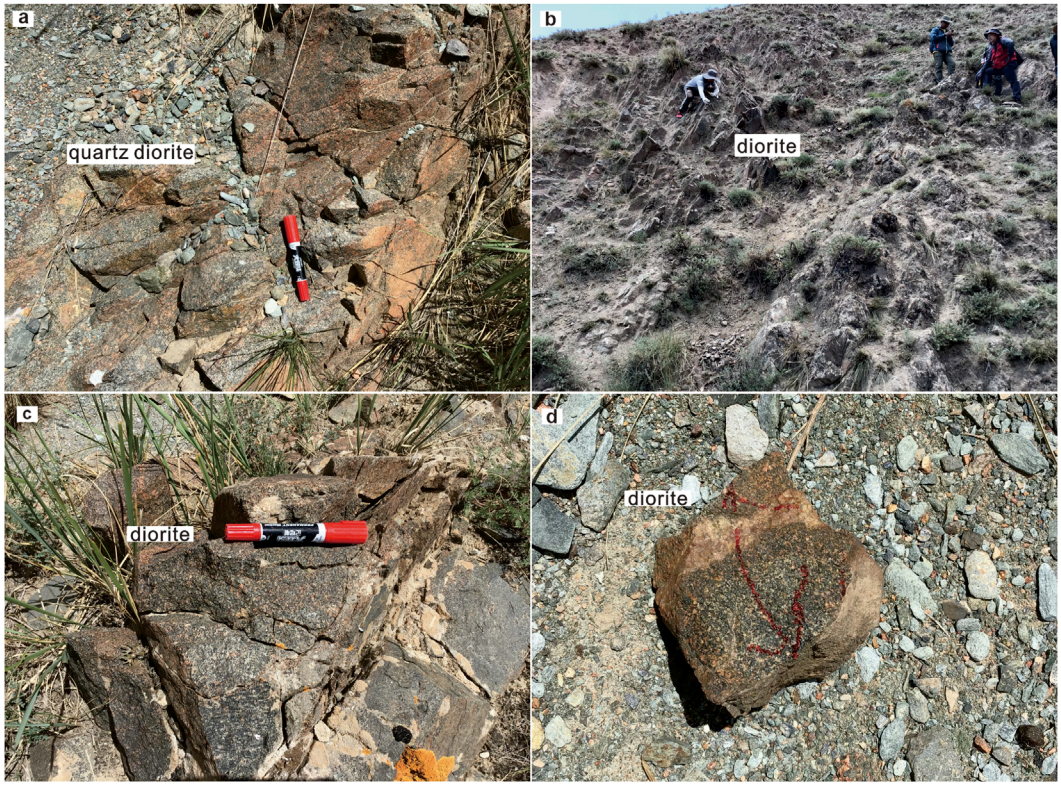

FIGURE 4
Field photographs of the Shandan quartz diorite and diorite in the Longshoushan region. Outcrops of **(a)** the Shandan quartz diorite, **(b-d)** the Shandan diorite.

in interstices between plagioclase grains. Accessory minerals include Fe–Ti oxides and apatite (Figures 5b, c).

3.2 Zircon U–Pb dating and Hf-O isotope

All analyses were carried out at the Guangxi Key Laboratory of Hidden Metallic Ore Deposit Exploration, Guilin University of Technology, Guangxi, China. We separated zircon grains from three diorites (21SD-282, 21SD-74 and 21SD-79) using conventional heavy-liquid and magnetic methods, which we mounted in epoxy resin and polished with 0.25 μm diamond paste. The internal textures of the grains were carefully examined using transmitted- and reflected-light photomicrographs as well as cathodoluminescence (CL) images. The CL imaging was performed using a JXA-8230 R electron microprobe.

Zircon U–Pb dating and trace element analyses were carried out simultaneously using laser ablation–inductively coupled plasma–mass spectrometry (LA–ICP–MS) comprising a quadrupole ICP–MS instrument (Agilent 7900) coupled to a GeoLas HD 193 nm ArF excimer laser with an automatic positioning system. The laser spots were 24 μm in diameter. Each analysis included ~20–30 s of background acquisition (using a gas blank) followed by 50 s of acquisition of U, Th, ^{204}Pb, ^{206}Pb, ^{207}Pb, and ^{208}Pb data from the sample. Trace element contents were calibrated using NIST 610 glass and Si as external and internal standards, respectively. Isotopic fractionation was corrected using Plešovice zircon as an external standard. ICPMSDataCal (Liu et al., 2008) was used to calculate trace element contents and U–Pb isotopic ratios. Concordia ages and diagrams were obtained using Isoplot/Ex (Ludwig, 2003).

Hf isotopic analyses of the same zircon grains were conducted using an ArF excimer LA system attached to a Neptune Plasma multi collector (MC)–ICP–MS with a beam diameter of 44 μm, 30 s of ablation, repetition rate of 6 Hz, and laser beam energy density of 6 J/cm^2. During data acquisition, the GJ-1 zircon standard was analyzed as an external standard to check the reliability and stability of the instrument.

Zircon oxygen isotope was measured using a Cameca IMS-1280-HR SIMS (secondary ion mass spectrometer) at the SKLaBIG, GIG-CAS. The detailed analytical procedures were similar to those described by Li et al. (2009) and Yang Q. et al. (2018). The $^{133}Cs^+$ primary beam was accelerated at 10 kV with an intensity of about 2 nA and a beam size of about 20 μm. A normal incidence electron gun was activated to compensate for sample charging during analysis. Mass resolution of ca. 2,500 was obtained with multi-collection mode. The nuclear magnetic resonance (NMR) probe was used for magnetic field control. Oxygen isotope ^{18}O and ^{16}O were measured in two off-axis Faraday cups H1 and L′2, respectively. Each spot analysis took less than 3 min consisting of pre-sputtering (ca. 30 s), automatic secondary beam centering (ca. 60 s) and integration of oxygen isotopes (4 s/cycle × 16 cycles).

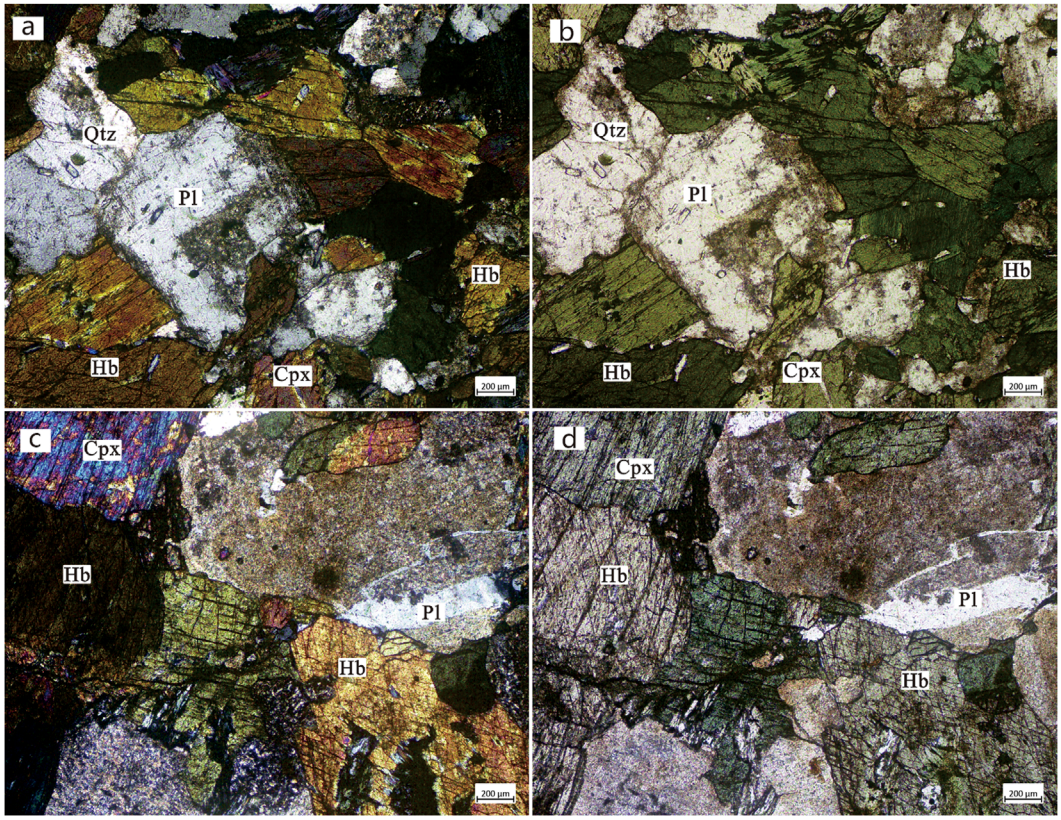

FIGURE 5
Photomicrographs of the Shandan intrusions. **(a, b)** Quartz diorite and **(c, d)** diorite. Pl: plagioclase, Cpx: clinopyroxene, Hb: hornblende, Qtz: quartz. a and c are cpl; b and d are ppl.

Measured $^{18}O/^{16}O$ ratios are reported as $\delta^{18}O$ per mil (‰) values calculated relatively to oxygen isotopic composition of Vienna Standard Mean Ocean Water $(^{18}O/^{16}O)_{VSMOW} = 0.0020052$ (Baertschi, 1976). The instrumental mass fractionation factor (IMF) for zircon was corrected using zircon standard Penglai (5.31‰, Li et al., 2010). All the fourteen measurements of the Qinghu zircon standard yielded a weighted-mean $\delta^{18}O$ values of 5.6‰ ± 0.1‰ (2σ), within errors of the reported value of 5.4‰ ± 0.2‰ (Li et al., 2013).

3.3 Whole-rock geochemistry

Five samples of fresh rock were selected and crushed into small chips. Any chips that were strongly altered or included secondary veins were removed, and the remaining chips were soaked in 4 N hydrochloric acid for 30 min to leach out alteration minerals. The rock chips were then powdered using an alumina ceramic shatter box. Major-element compositions were determined using a ZSX Primus II X-ray fluorescence spectrometer. Calibration lines used in quantification were produced by bivariate regression of data from 36 reference materials encompassing a wide range of silicate compositions (Li et al., 2005). Analytical uncertainties are between 1% and 5%. The loss on ignition (LOI) of each sample was measured before major-element analyses, which were carried out after calcination.

Trace-element analyses were performed using an Agilent 7500CX ICP–MS instrument, employing the acid-solution method of (Liu et al., 2021). First, ~50 mg of sample powder was placed in a bomb, and 0.5 mL of purified HNO_3 and 1.0 mL of HF were added. The bomb was then placed in a high-pressure valve at 190°C for 48 h. After evaporation, 0.5 mL of purified HNO_3 was added to the bomb, and this step was repeated. Subsequently, 4 mL of purified 4 N HNO_3 was added to the bomb, which was then placed in the high-pressure valve at 170°C for 4 h. Finally, the solution was diluted 1,000 times, and 10 ppb of Rh was added as an internal standard to correct for instrument drift.

Sr–Nd–Pb isotopic compositions were determined using the method of Zhang Z. G. et al. (2021). The sample powder was dissolved in a Savillex Teflon cup by adding 2 mL of 22 N HF and 1 mL of 8 N HNO_3, and then heated to 120°C on a hot plate for 5–7 days. After drying, 3 mL of HNO_3 was added to dissolve the sample again. Sr was separated using SR-B50-A (100–150 μm) resin. Rare earth elements (REEs) were separated with AG 50-X8 cation exchange resin, and Nd was purified with HDEHP resin. Blanks contained <300 pg of Rb and Sr, and <100 pg of Sm and Nd. Mass fractionation was corrected by assuming an $^{88}Sr/^{86}Sr$ ratio of 8.375209 and a $^{146}Nd/^{144}Nd$ ratio of 0.7219. Instrument stability was monitored using NBS-987 and JNdi-1 standard solutions for Sr and Nd isotopic compositions, respectively. Repeated analyses of NBS-987 and JNdi-1 yielded a mean $^{87}Sr/^{86}Sr$ ratio of 0.710294 ±

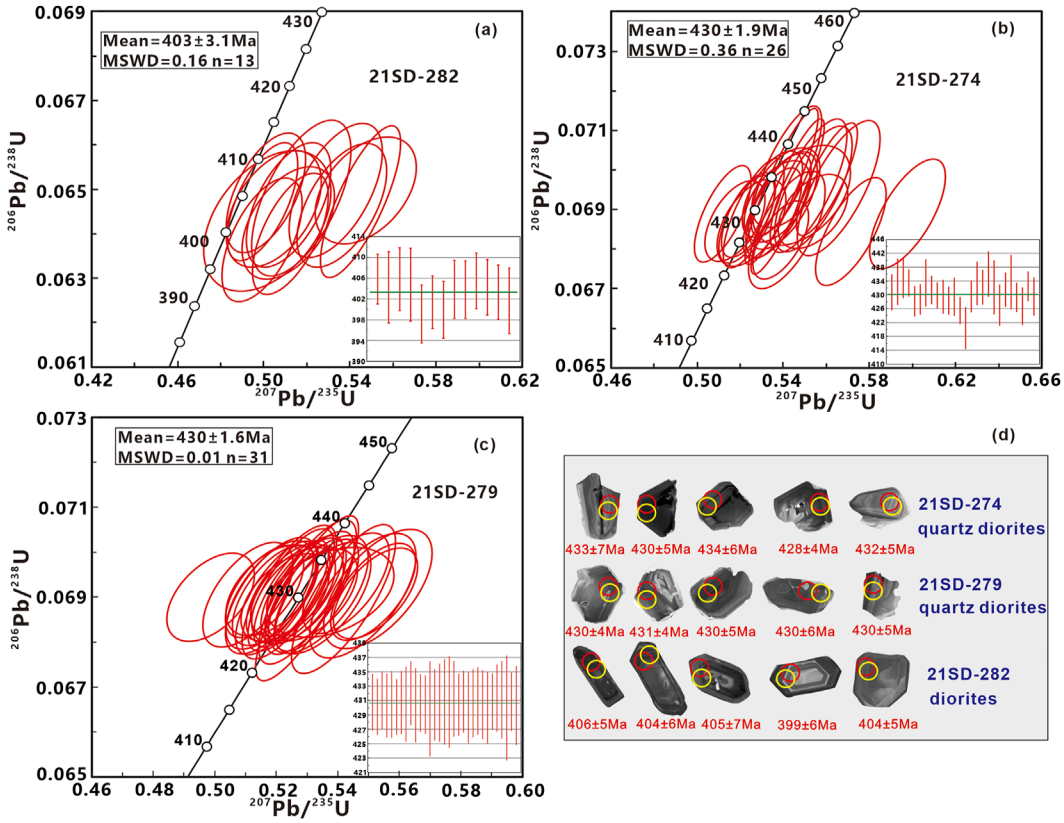

FIGURE 6
(a–c) U–Pb concordia diagrams for the analyzed samples and **(d)** cathodoluminescence images of representative zircon grains.

0.000016 (n = 40, 2 SD) and a mean $^{143}Nd/^{144}Nd$ ratio of 0.512081 ± 0.000008 (n = 40, 2 SD), respectively. The mean measured $^{87}Sr/^{86}Sr$ and $^{143}Nd/^{144}Nd$ ratios of BHVO-2 were 0.703549 ± 0.000008 and 0.512965 ± 0.000004, respectively.

Lead was extracted by placing sample powders in Teflon beakers and dissolving by adding 3 mL of concentrated HF and 1 mL of concentrated HNO_3, then heating at 120°C for 5–7 days. Lead was purified using the conventional cation exchange technique (AG 1-X8, 200–400 resin) with diluted HBr as an eluant. The total procedural blanks contained <50 pg of Pb.

4 Results

4.1 Zircon U–Pb geochronology and zircon Hf–O isotopic compositions

We selected three intrusive rocks from Shandan, including diorite and quartz diorite, for zircon U–Pb age and Hf-O isotopic analyses (Figures 6, 7). The results of the zircon U–Pb geochronology and Hf-O isotopic analyses are listed in Supplementary Tables S1–S3, and the representative zircon CL images are presented in Figure 6d. Zircon grains from the three samples are euhedral, and most have lengths of 150–200 μm and widths of 80–140 μm. All the analyzed grains have euhedral concentric zoning and high U (431–9,800 ppm) and Th (43.2–11,492 ppm) contents and Th/U ratios (0.08–1.48), suggesting an igneous origin for the zircon grains and that their U–Pb ages represent the timing of crystallization of the Shandan intrusive rocks (Hoskin and Black, 2000).

The diorite sample 21SD-282 yielded a weighted mean $^{206}Pb/^{238}U$ age of 403 ± 3.1 (1σ, MSWD = 0.16), suggesting that it crystallized during the Early Devonian. The $\varepsilon_{Hf}(t)$ values are variable, ranging from +2.24 to −11.0, with T_{DM} model ages of 1,271–927 Ma (Figure 6a). Zircon grains from the quartz diorite samples 21SD-274 and 21SD-279 yielded weighted mean $^{206}Pb/^{238}U$ ages of 430 ± 1.6 (1σ, MSWD = 0.01) and 430 ± 1.9 (1σ, MSWD = 0.36), respectively (Figures 6b, c), suggesting that they crystallized during the middle Silurian. Their $\varepsilon_{Hf}(t)$ values are variable, ranging from +0.14 to +6.58, with T_{DM} model ages of 1,023–751 Ma (Figure 7a). *In situ* zircon Hf–O isotopic data for the quartz diorite sample 21SD-279 are listed in Supplementary Table S5. The quartz diorite has intermediate zircon $\delta^{18}O$ values (5.75‰ ± 0.18‰–6.38‰ ± 0.18‰) and variable zircon $\varepsilon_{Hf}(t)$ values (+0.08 to +3.55), with two-stage Hf model ages of 1,416–1,196 Ma (Figure 7; Supplementary Table S5).

4.2 Whole-rock major and trace elements

The major and trace element compositions of the studied Shandan diorites are listed in Supplementary Table S4 and

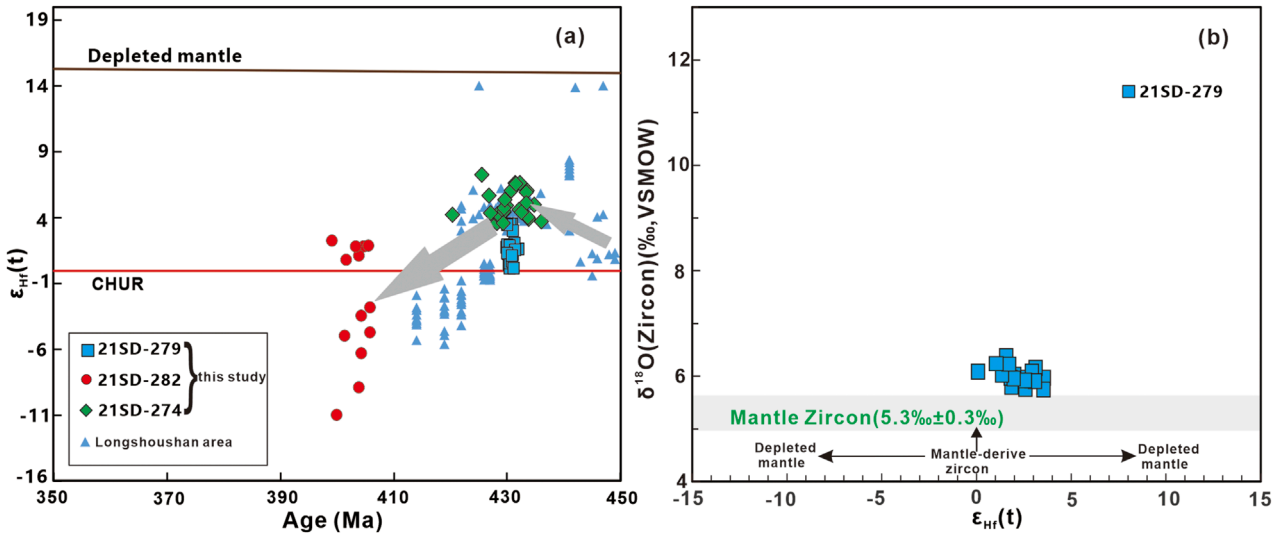

FIGURE 7
(a) Zircon $\varepsilon_{Hf}(t)$ values versus age (Zhang L. Q. et al., 2021; Zhang L. Q. et al., 2017) and **(b)** zircon O–Hf isotopic composition diagrams for the quartz diorites and diorites in the Shandan area. The mean zircon $\delta^{18}O$ value of mantle magmas (5.3‰ ± 0.3‰, 1σ) is from Valley et al. (1998).

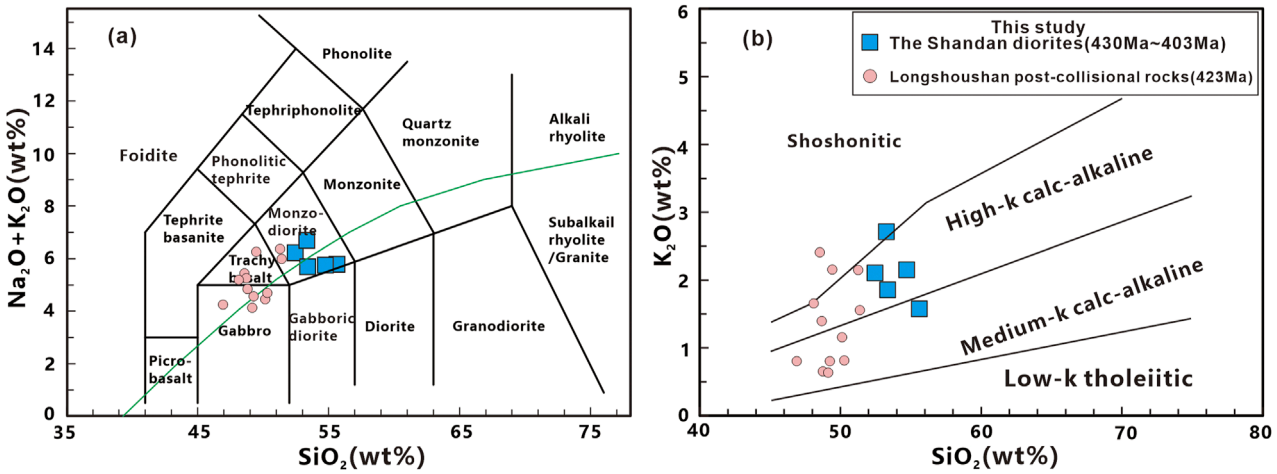

FIGURE 8
Major element discrimination diagrams for the Shandan diorites. **(a)** Total alkali (Na_2O+ K_2O) versus SiO_2 diagram (after Maitre et al., 1986). **(b)** K_2O versus SiO_2 diagram (after Gill, 1981). Data for the Longshoushan post-collisional rocks are from Duan et al. (2015).

shown in Figures 8, 9. The LOI values for the sampled analyzed in this study were 2.21–2.69 wt%. All major oxide contents were normalized to LOI-free values before interpretation.

The Shandan diorites are characterized by intermediate SiO_2 contents (52.47–55.69 wt%) and relatively high Al_2O_3 (16.57–18.49 wt%), CaO (5.99–7.29 wt%) and MgO (3.91–4.66 wt%) contents, with Mg# (Mg# = 100 × M Mg/[Mg + Fe^{2+}]) of 48.2–59.4 and Na_2O + K_2O contents of 1.74–5.50 wt%. The rocks plot in the monzodiorite field on a total alkali versus silica diagram (Figure 8a). All rocks plot along the medium to high-K calc-alkaline series on a SiO_2 versus K_2O diagram (Figure 7b).

The rocks yield a restricted range of trace element contents. Chondrite-normalized REE patterns show enrichment in light REEs (LREEs) relative to heavy REEs (HREEs), with $(La/Yb)_N$ ratios of 12.7–23.6. The samples are also characterized by weakly negative Eu anomalies (Eu/Eu^*= 0.91–0.97), suggesting slight fractionation of plagioclase during crystallization (Figure 9a). They show a remarkable enrichment in large-ion lithophile elements (LILEs; e.g., Ba and U) and depletion of high field strength elements (HFSEs; e.g., Nb, Ta, and Ti) on a primitive-mantle-normalized trace element diagram (Figure 9b), similar to subduction-related magmas. They have high Sr contents (192–374 ppm), low Y contents (192–374 ppm), and high Sr/Y ratios (11–25).

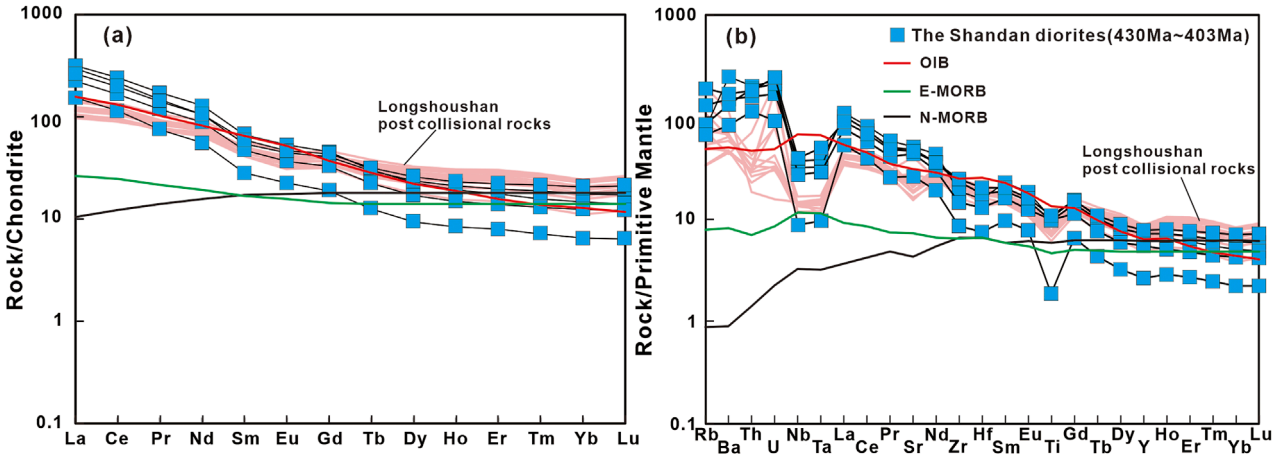

FIGURE 9
(a) Chondrite-normalized REE and **(b)** primitive-mantle-normalized trace element diagrams for the Shandan intrusive rocks. Chondrite and primitive mantle values are from Sun and McDonough (1989); Data for the Longshoushan post-collisional rocks are from Duan et al. (2015).

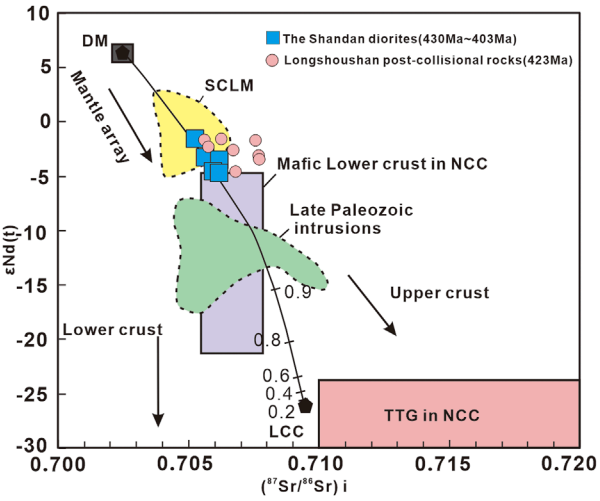

FIGURE 10
$\varepsilon_{Nd}(t)$ vs. $^{87}Sr/^{86}Sr$ ratios for Shandan diorites, showing mixing trends between depleted mantle and lower crustal components. (Fu et al., 2020; Zhang et al., 2023). Data for the late Paleozoic intrusions on the northern margin of the North China Craton (NCC) are from Wu et al. (2006) and Zhang et al. (2018). Data for the Longshoushan post-collisional rocks are from Duan et al. (2015); The composition of the subcontinental lithospheric mantle (SCLM) beneath the NCC was estimated using xenoliths and perovskites in Paleozoic kimberlites (Yang et al., 2009). DM: depleted mantle (Workman and Hart, 2005). Data for Archean mafic lower crust and TTG gneisses in the NCC are from Chen et al. (2014) and Griffin et al. (2002).

4.3 Whole-rock Sr–Nd–Pb isotopic compositions

The whole-rock initial Sr–Nd–Pb isotopic compositions of the Shandan diorites are listed in Supplementary Table S5 and shown in Figure 10. Their $(^{87}Sr/^{86}Sr)_i$ ratios and $\varepsilon_{Nd}(t)$ values were calculated using crystallization ages of 430–403 Ma (Figure 9). All samples yield a limited range of $(^{87}Sr/^{86}Sr)_i$ ratios (0.705247–0.706181) and $\varepsilon_{Nd}(t)$ values (−1.58 to −4.74), with two-stage Nd model ages of 1,374–1,447 Ma. The age-corrected Pb isotopic ratios of these diorites are variable, with $^{206}Pb/^{204}Pb(t)$ ratios of 17.996–18.225, $^{207}Pb/^{204}Pb(t)$ ratios of 15.566–15.576, and $^{208}Pb/^{204}Pb(t)$ ratios of 37.943–38.126. In plots of $^{207}Pb/^{204}Pb(t)$ and $^{208}Pb/^{204}Pb(t)$ versus $^{206}Pb/^{204}Pb(t)$ (Figure 11), all the samples plot above the Northern Hemisphere reference line and have similar isotopic compositions to those of typical Indian MORB.

5 Discussion

5.1 Petrogenesis for the shandan diorite

The relatively high LILE and LREE contents of the Shandan diorites suggest they were contaminated by continental crust; therefore, before discussing the source of magma, we must assess whether crustal contamination occurred during their formation. The Zr/Nb ratios of most samples (8.32–15.6) are lower than that of the continental crust (11.43; Rudnick and Gao, 2003), with only sample 21SD-279 having a higher Zr/Nb ratio. All samples lack older inherited zircon grains, and their relatively homogeneous zircon Hf isotopic compositions indicate a limited extent of crustal contamination. In addition, the narrow range of SiO_2 contents in the Shandan diorites suggests limited magma mixing during their evolution.

The Mg# (48–59) and Cr (5–63 ppm) and Ni (6.6–15.9 ppm) contents of the Shandan diorites are relatively low, below those of primitive-mantle-derived magmas (Mg# = 68–76, Cr = 300–500 ppm, Ni = 300–400 ppm; Hess, 1992). This suggests they experienced fractional crystallization. The variations in TiO_2 (1.09–2.04 wt%) and Fe_2O_3T (7.42–10.19 wt%) contents are small, with a weak Ti anomaly (Figures 9a, b), indicating that Fe–Ti oxides were not a significant fractionating phase during crystallization. The Eu (Eu/Eu*= 0.91–0.97) and Sr

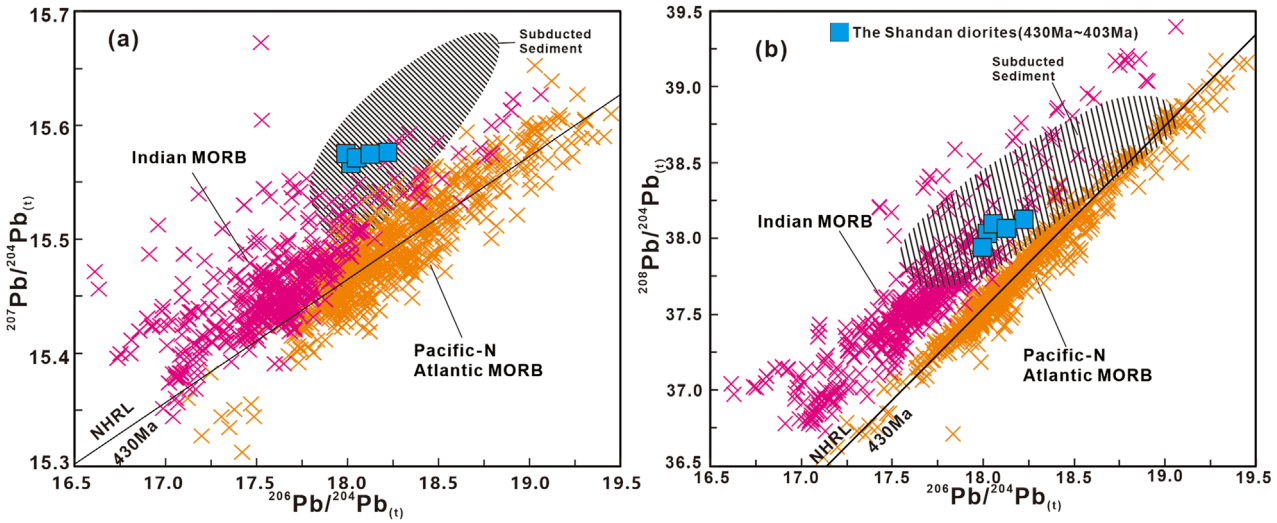

FIGURE 11
Age-corrected **(a)** $^{207}Pb/^{204}Pb(t)$ and **(b)** $^{208}Pb/^{204}Pb(t)$ versus $^{206}Pb/^{204}Pb(t)$ ratios of diorites (430 Ma) from the Shandan area. Data for present-day Pacific–North Atlantic and Indian MORB are from the PetDB database (http://www.petdb.org/) and the compilation of Liu et al. (2014). Subducted sediments are from Plank and Langmuir (1998); Vervoort and Blichert-Toft (1999); Vervoort et al. (2011). The Northern Hemisphere reference line (NHRL) is from Hart (1984).

anomalies of the Shandan diorites are small, indicating negligible fractionation or accumulation of plagioclase. The Ni content is nearly constant, and the positive correlation between V and Cr contents suggests that the petrogenesis of the Shandan diorites was dominated by the fractional crystallization of clinopyroxene and hornblende (Zhang et al., 2023; Figures 12a, b).

The zircon ages (430–403 Ma) of the studied Shandan diorites indicate they formed during the middle Silurian and Early Devonian. The diorites have island-arc-like trace element compositions, with enrichment in LILEs and LREEs and depletion in HFSEs (Figure 9). The samples have low Nb/La (0.24–0.29), Nb/Th (1.04–3.31), and Nb/U (5.13–10.01) ratios, similar to subduction-related magmas and Longshoushan post-collisional rocks (Dilek and Furnes, 2014; Duan et al., 2015; Pearce et al., 2014). Magma can be produced in a subduction-related environment by (a) the release of fluids during dehydration of the subducting oceanic slab, (b) partial melting of sediments from the oceanic slab, and (c) partial melting of the oceanic slab itself (Tatsumi and Takahashi, 2006). Direct melting of the oceanic slab is unlikely in the present case, because it is often accompanied by the formation of adakites, an intermediate rock characterized by low Y and high Sr contents, and LREE-enriched REE patterns (Defant and Drummond, 1990). In contrast, the diorites of this study have low Sr/Y ratios and high Y contents and similar to Longshoushan post-collisional rocks (Figure 12c; Duan et al., 2015). Therefore, we suggest that these diorites were not derived through the direct partial melting of the oceanic slab. The enrichment of the studied rocks in LILEs and LREEs relative to HFSEs and HREEs suggests they were associated with subducted material (Figure 9; Pearce and Parkinson, 1993). The Shandan diorites have low and uniform Ce/Pb ratios, but variable Th/La ratios (Figure 12d), suggesting a significant input of sediment or sediment-derived melt into their source. The Th contents of sediments are more than two orders of magnitude greater than that of the mantle (Hawkesworth et al., 1997; Plank and Langmuir, 1998); therefore, the addition of sediment-derived melt to a source result in increasing Th/Yb ratios but has little effect on Ta/Yb ratios (Pearce, 2008). We can use the Th/Yb and Ta/Yb ratios help constrain the magma source of Shandan diorites, as they remain stable during partial melting and fractional crystallization (Pearce and Peate, 1995). The Shandan diorites yield a narrow range of Th/Yb and Ta/Yb ratios (Figure 12e). The Th/Yb ratio of all samples are higher than those of the MORB–ocean island basalt (OIB) array, implying that the Shandan diorites added the subducted sediment melt elevated the Th abundance in the source. This suggests that contributions from subduction-related sediment-derived melts to their source.

The Shandan diorites are characterized by high MgO (3.91–4.66 wt%) and Mg# (48–59), Cr (5.18–63.3 ppm) and Ni (7.1–46.8 ppm) contents. In contrast, their SiO_2 contents (52.48–50.72 wt%) are lower than that of the continental crust (SiO_2 = 60.6 wt%), suggesting the incorporation of mantle-derived components (Pearce et al., 2014). LILEs and LREEs are enriched in the samples, with high Sr contents and Th/U ratios (2.81–4.79), similar to the incompatible element enrichment in the lithospheric mantle (Hawkesworth et al., 1993; Liu et al., 2023). This enrichment can be attributed to metasomatic processes associated with subduction or partial melting. In addition, the Shandan diorites yield high La/Nb ratios (3.43–4.41) and low La/Ba ratios (0.02–0.06) (Figure 12f), similar to subcontinental lithospheric mantle melts influenced by subduction (Thompson et al., 2008). Therefore, it is plausible that the Shandan diorites originated from an enriched source in

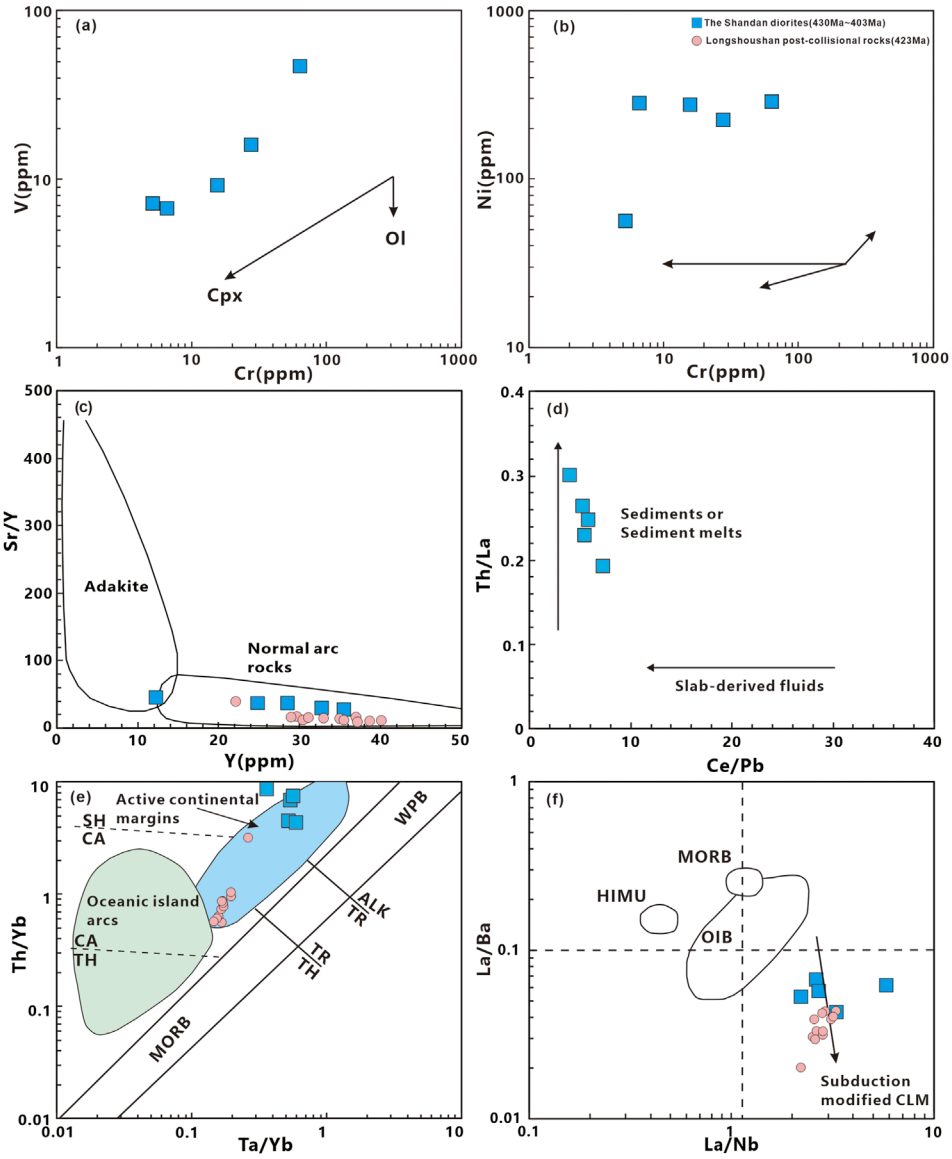

FIGURE 12
(a) V versus Cr, **(b)** Ni versus Cr, **(c)** Sr/Y versus Y (Defant and Drummond, 1990), **(d)** Th/La versus Ce/Pb (Mazza et al., 2020), **(e)** Th/Yb versus Ta/Yb (Pearce and Peate, 1995), and **(f)** La/Ba versus La/Nb diagrams for the Shandan diorites (Saunders et al., 1992). MORB, mid-ocean ridge basalt; WPB, within-plate basalt; SH, shoshonite; CA, calc-alkaline; TH, tholeiite; ALK, alkaline; TR, transitional. Data for the Longshoushan post-collisional rocks are from Duan et al. (2015); The reference fields for OIB, MORB, and high-U/Pb mantle (HIMU) sources are from Saunders et al. (1992).

subcontinental lithospheric mantle and similar to Longshoushan post-collisional rocks (Duan et al., 2015).

The whole-rock Sr–Nd–Pb and zircon Hf isotopic data further constrain the characteristics of the mantle source of the Shandan diorites. The Shandan diorites yield enriched Sr and Nd isotopic compositions, with high initial $^{87}Sr/^{86}Sr$ ratios (0.705,247–0.706,181) and variable initial $\varepsilon_{Nd}(t)$ values (−1.58 to −4.74). Their Sr–Nd isotopic signature suggests the possible incorporation of subcontinental lithospheric mantle and the mafic lower crust into their magma source, similar to the Longshoushan post-collision rocks (Duan et al., 2015). The samples yield a narrow range of $^{207}Pb/^{204}Pb(t)$ and $^{208}Pb/^{204}Pb(t)$ ratios. Due to the mobility of Pb, the Pb isotopic composition of the mantle can be altered by the addition of slab-derived fluids or sedimentary melts, allowing us to identify subducted-sediment-derived melts in the mantle source (Liu et al., 2014; Liu et al., 2021b; Pearce and Peate, 1995). On $^{207}Pb/^{204}Pb(t)$ versus $^{206}Pb/^{204}Pb(t)$ and $^{208}Pb/^{204}Pb(t)$ versus $^{206}Pb/^{204}Pb(t)$ diagrams (Figures 11, 13a), the Shandan diorites fall in the overlapping Indian Ocean MORB and subducted sediment fields, suggesting an Indian Ocean MORB-like source with the incorporation of subducted sediment.

Moreover, as the sediments have undergone surface weathering, they yield considerably higher $\delta^{18}O$ values (>8.0‰) than those of the mantle ($\delta^{18}O$ = 5.3‰ ± 0.3‰; Li et al., 2009). Zircons derived from the Earth's mantle typically have $\delta^{18}O$ values

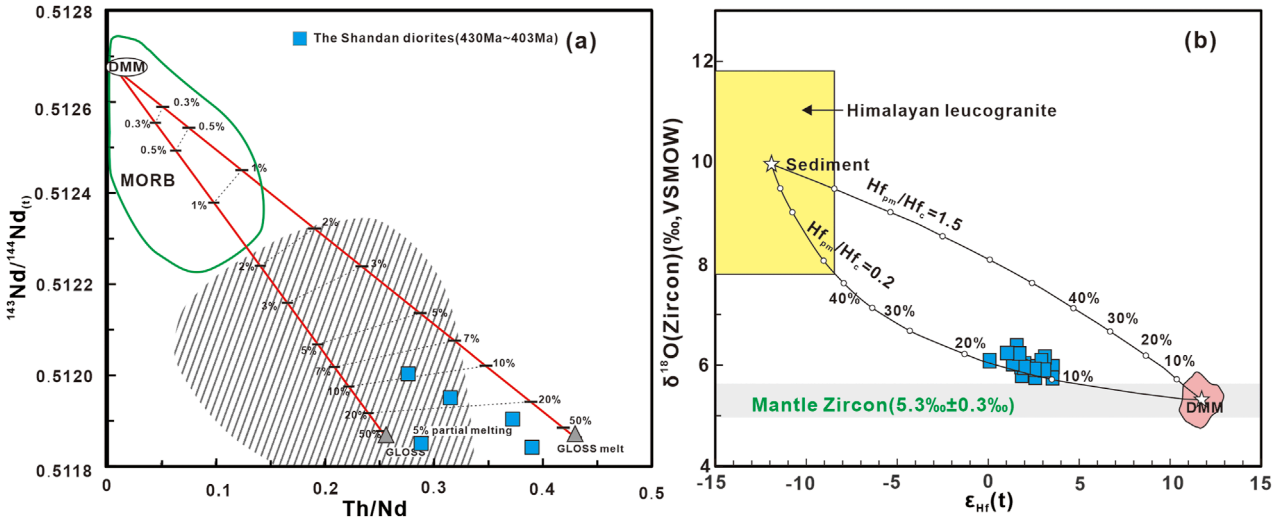

FIGURE 13
(a) $^{143}Nd/^{144}Nd(t)$ versus Th/Nd diagram for the Shandan diorites, showing mixing models between GLOSS or GLOSS melt and DMM. **(b)** *In situ* zircon $\varepsilon_{Hf}(t)$ versus $\delta^{18}O$ values (modified from Li et al., 2009). Data for subducted sediment are from Nowell et al. (1998); Plank and Langmuir (1998); Vervoort et al. (2011). The fields for present-day Pacific–North Atlantic and Indian MORB are from Liu et al. (2014), DMM trace element contents are from Workman and Hart (2005), and sediment/melt and sediment/fluid partition coefficients are from Johnson and Plank (2000).

between approximately 5.3‰ ± 0.3‰ (Li et al., 2009). For Shandan diorites, the $\delta^{18}O$ values of zircon between 5.75‰ and 6.38‰ is generally indicating the primary source remained mantle-derived, but the slight enrichment in $\delta^{18}O$ in zircons within the diorite suggests the mantle source partially influenced by subduction components or crustal contamination (Figure 7b). On a zircon Hf–O isotopic diagram, the Shandan intrusive rock plots between the Qinghu monzogranite (representing mantle O isotopic compositions; Li et al., 2009) and Himalayan leucogranite (representing sedimentary O isotopic compositions (Hopkinson et al., 2017; Figure 13b), indicating the incorporation of sediment into its source. Therefore, it is highly likely that the Shandan diorites originated from an enriched subcontinental lithospheric mantle source metasomatized by subducted-sediment-derived melts.

In addition, the zircon ages and Hf isotopic compositions of the Shandan diorites suggest two stages of magmatism with different sources (Figure 7a). The zircon grains from the first stage (430 Ma) yield initial $\varepsilon_{Hf}(t)$ values ranging from moderately positive (+0.14) to highly positive (+6.58), with model ages of 1,023–751 Ma, suggesting that they were derived predominantly from enriched mantle components with only a minor crustal contribution. The zircon grains from the second stage (403 Ma) yield negative $\varepsilon_{Hf}(t)$ values (2.24 to −11.0), with model ages of 1,271–927 Ma, suggesting that the magma was influenced primarily by the addition of Mesoproterozoic to Neoproterozoic crustal material and mixed with the enriched mantle components source (Zhang L. Q. et al., 2017). Therefore, the zircon Hf isotopic characteristics of the Shandan diorites with ages of 430–403 Ma indicates a decrease in the contribution of enriched mantle material and a greater incorporation of continental crustal material (Jahn et al., 1999). In conclusion, the trace element and isotopic data suggest that the Shandan diorites originated from the enriched subcontinental lithospheric mantle mixed with crustal material melts.

The trace element and isotopic data suggest that the Shandan diorites were formed by the partial melting of enriched subcontinental lithospheric mantle contaminated with a mixture of subduction-related sediment-derived melts and crustal material. We further discuss the nature of the contributions from sediment and the mafic lower crust. We used a two-endmember $^{87}Sr/^{86}Sr$ versus $\varepsilon_{Nd}(t)$ mixing model to quantitatively estimate the contribution of crustal material to the Shandan samples (Figure 10). We selected lower continental crust (LCC; Jahn et al., 1999) as the crustal endmember and depleted mantle (DM) as the mantle endmember (Workman and Hart, 2005; Zindler and Hart, 1986). The results indicate that the basaltic magma consists of ~95%–94% DM-derived material and ~5%–6% LCC magma.

We evaluated the contribution of sediment-derived melt using $^{143}Nd/^{144}Nd(t)$ versus Th/Nd ratios and the zircon Hf–O isotopic composition of the endmember of the two-component mixing model for the Shandan diorites (Figure 13). Th and Nd are not mobile in fluid released during the dehydration of subducted oceanic crust and sediment, but are mobile in sediment-derived melt (Class et al., 2000; Johnson and Plank, 2000; Plank and Langmuir, 1998); therefore, we calculated the range of Th/Nd ratios at a given $^{143}Nd/^{144}Nd$ value that would be produced by the mixing of global bulk subducted sediment (GLOSS; Plank and Langmuir, 1998) and partial melts of sediment with depleted mantle MORB (DMM; Figure 13a; Liu et al., 2014). The results show that mixing bulk GLOSS and DMM cannot produce the high Th/Nd ratios of the Shandan diorites (Figure 13a); however, <5% partial melting of GLOSS yielded the Th/Nd and $^{143}Nd/^{144}Nd(t)$ ratios of the Shandan diorites. A Hf–O isotopic mixing model using the Qinghu monzonite as the mantle

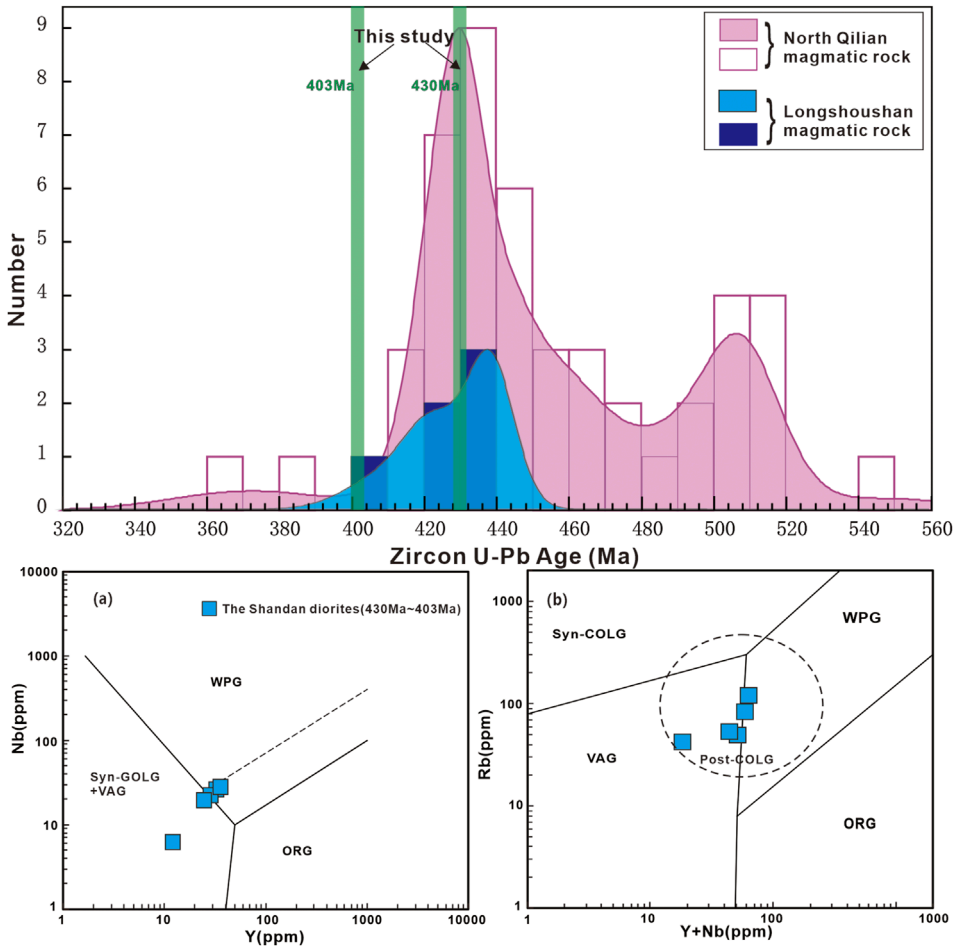

FIGURE 14
(a) Ages of Paleozoic magmatic rocks in the North Qilian and Longshoushan areas. Age data are listed in Supplementary Table S6; **(b)** Rb versus Y + Nb (after Pearce, 1996) and **(c)** Nb versus Y (after Eby, 1992) diagrams for the Shandan diorites. ORG: ocean ridge granitoid, syn-COLG: syn-collisional granitoid, VAG: volcanic arc granitoid, WPG: within-plate granitoid.

endmember and Himalayan leucogranite as the sedimentary endmember also suggests that the source of the Shandan diorites contains 10%–20% sediment (Li et al., 2009; Figure 13b). Thus, the addition of 10%–50% sediment-derived partial melt to a DMM source can produce the parental magmas of the Shandan diorites.

5.2 Implication for the timing of slab breakoff

Orogenic processes in the region between the NQOB and Alxa Block generated intermediate to felsic magmas during various stages of convergence, including during the oceanic subduction, arc–continent collision, post-collision, and continental subduction stages (Song et al., 2014; Song et al., 2007; Zhang L. Q. et al., 2017). This magmatic activity provides important insights into the relationship between geodynamic processes and tectonic evolution, improving our understanding of the interactions between the asthenosphere, lithospheric mantle, and continental crust (Dewey, 1988). Previous studies on the intermediate to felsic magmatic rocks, including diorite and granite in the Longshoushan Belt on the southwestern margin of the Alxa Block, suggested a close association with collision between the Alxa and Qilian–Qaidam blocks and post-collisional extension resulting from the continued subduction of the early Paleozoic North Qilian oceanic crust (Fu et al., 2019; Kang et al., 2018; Yang X. Q. et al., 2018). During the Cambrian–Silurian, the North Qilian oceanic crust was subducted northward beneath the Alxa Block, leading to back-arc extension in the NQOB (Xia et al., 2012). The lithospheric mantle was extensively metasomatized by fluids and melts derived from the oceanic crust and sediments. This process resulted in the formation of early Paleozoic intermediate to felsic magmatic rocks in the oceanic crust and subcontinental lithospheric mantle beneath the Alxa Block, as observed in the North Qilian belt (Qian et al., 2001; Song et al., 2013; Xia et al., 2003). Therefore, we can review the tectonic evolution of the Longshoushan and Shandan areas by considering the early Paleozoic intermediate to felsic magmatic rocks from the North Qilian and Longshoushan regions.

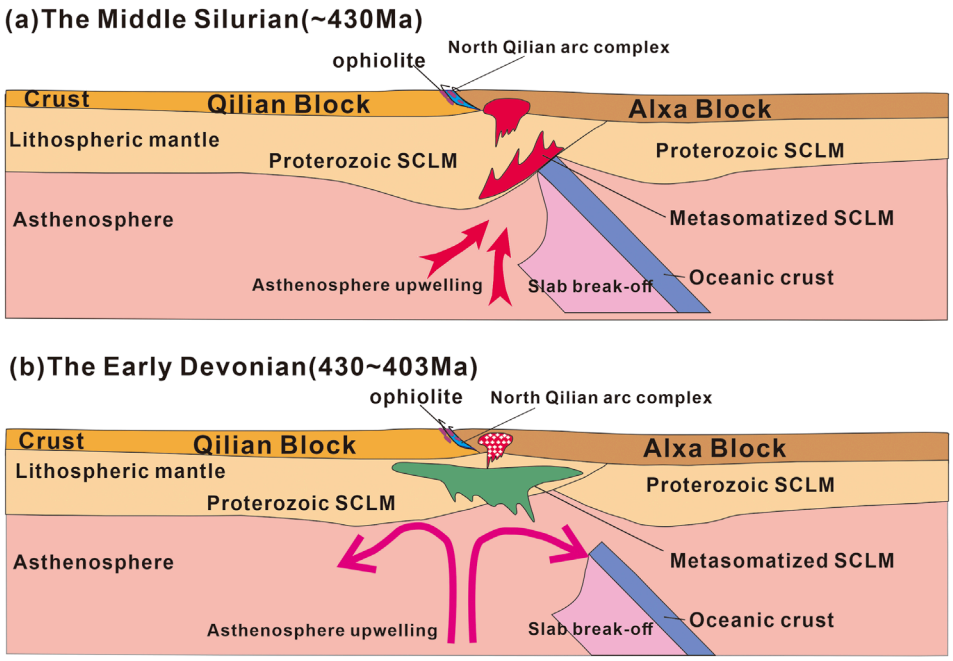

FIGURE 15
Tectonic model for the Shandan area between the middle Silurian and Early Devonian in the North Qilian Orogenic Belt and Alxa Block. **(a)** Slab break-off occurred around 430 Ma, creating a window for upwelling asthenospheric material; **(b)** Slab break-off was nearing end at 403 Ma, leading to weaker asthenospheric upwelling. SCLM, subcontinental lithospheric mantle.

Figure 14a compares the timing of Paleozoic magmatic activity in the North Qilian and Longshoushan regions. Previous studies of the intermediate to felsic magmatic rocks in the Longshoushan area of the Alxa Block focused mainly on the Jinchuan quartz syenite (433 Ma; Zeng et al., 2016) and the fine-grained Qingshanbao granite (430 Ma; Liu et al., 2019), and inferred that these rocks formed in a post-collisional intraplate extensional environment. The Dafusi alkali feldspar granite in the western segment of the Longshoushan Belt formed during the late Silurian (426 ± 2 Ma) in a post-collisional extensional environment, as did the Silurian Hexibao granite in the eastern segment of the Longshoushan Belt (Fang et al., 1997). Previous studies of the intermediate to felsic magmatic rocks in the NQOB examined the 516–505 Ma high-Al Chaidanuo granite (Chen et al., 2014), the 501 Ma Kekeqi quartz syenite, the 477 Ma Niuxinshan granite, and the 457–441 Ma adakitic granite (Tseng et al., 2009; Yu et al., 2015; Zhang L. Q. et al., 2017), which are associated with the formation of oceanic crust and subduction–accretion processes. During this period (516–441 Ma), magmatic rocks were generated through the partial melting of oceanic crust during the initial stages of northward subduction of the Qilian oceanic crust (Wu et al., 2011; Wu et al., 2010; Wu et al., 2004). Studies of the 430 Ma Laohushan granite, 427 Ma Laohushan diorite, 424 Ma Jinfosi S-type granite, and 427–414 Ma Wuwei-Jinchang pluton (Chen et al., 2016; Tseng et al., 2009; Zhang L. Q. et al., 2017) suggest that the Alxa Block was in a syn-collisional or post-collisional setting along with the Central Qilian-Qaidam Block duirng 435–414 Ma. Furthermore, younger post-orogenic granites (~403–374 Ma) occur in the northern part of the NQOB (Song et al., 2013; Wu et al., 2010; Wu et al., 2004). Previous studies of the intermediate to felsic magmatic rocks in the Longshoushan and North Qilian areas suggest that the Shandan diorites (430–403 Ma) formed in a post-collisional environment associated with the final closure of the North Qilian Ocean and collision between the Alxa and Qilian blocks.

Magmatic activity during the post-collisional stage is associated with slab breakoff and lithospheric delamination. These processes lead to upwelling of the asthenosphere, providing a source of material and heat for post-collisional magmatic activity (Bird, 1979; Huw Davies and von Blanckenburg, 1995). The trace element contents (e.g., enriched LILEs, depleted HFSEs) and Sr–Nd–Pb–Hf–O isotopic compositions of the Shandan intrusions suggest that they formed through the partial melting of enriched subcontinental lithospheric mantle and the incorporation of crustal material and subduction-related sediment-derived melts. The tectonic setting of the Shandan intrusions can be constrained further using Rb versus Y + Nb and Y versus Nb discrimination diagrams (Pearce, 1996; Pearce and Peate, 1995; Figures 14b, c). In these diagrams, the Shandan diorites plot in the transitional zone between within-plate and island arc settings, as well as in the post-collision area, suggesting that they formed in post-collisional extension. These features align with slab breakoff models, where detachment of the subducted oceanic slab triggered asthenospheric upwelling, heating the overlying SCLM and facilitating partial melting (von Blanckenburg and Davies, 1995; van Hunen and Miller, 2015). Moreover, previous studies on the A-type granites magmatic activity in the Longshoushan Jinchuan regions suggest that asthenospheric upwelling was triggered by the post-collisional slab breakoff of the northern Qilian oceanic crust (433 Ma; Zeng et al., 2016). Therefore, we infer that the Shandan intrusions formed during post-collisional

slab breakoff, which created a window for upwelling asthenospheric material, inducing partial melting of the subcontinental lithospheric mantle and crust. Zircon Hf isotopes further constrain the timing and duration of slab breakoff. The gradual decline in mean $\varepsilon_{Hf}(t)$ values from +6.85 at 430 Ma to +1.2 at 403 Ma (Figure 15) reflects waning mantle input, possibly due to the end of slab detachment and weaker asthenospheric upwelling leading to a gradual decrease in crust–mantle interaction. This isotopic trend correlates with the cessation of magmatic activity by ~403 Ma, suggesting slab breakoff concluded by this time.

In summary, subduction of the North Qilian oceanic crust led to the consumption of oceanic crust and eventual collision between the Alxa and Central Qilian blocks at ~440 Ma (Song et al., 2014; Song et al., 2013; Xia et al., 2003). Due to differences in density, slab breakoff occurred around 430 Ma, creating a window for upwelling asthenospheric material and inducing the partial melting of subcontinental lithospheric mantle and crust. At ~403 Ma, slab breakoff was nearing end, leading to weaker asthenospheric upwelling. This model is consistent with global examples, where slab break-off has driven short-lived (<30 million years) post-collisional magmatic activity (von Blanckenburg and Davies, 1995). Thus, the Shandan diorites serve as a chronometer for slab detachment in the NQOB, constraining its onset to approximately 430 Ma and cessation by around 403 Ma.

6 Conclusion

We studied the petrology, geochronology, whole–rock geochemistry, Sr–Nd–Pb isotopic compositions, and zircon Hf–O isotopic compositions of the Shandan diorites in the Longshoushan area, allowing us to draw the following conclusions. The Shandan diorites consist mainly of middle Silurian (430 Ma) quartz diorites and Early Devonian (403 Ma) diorite. The intermediate $\varepsilon_{Nd}(t)$, zircon $\varepsilon_{Hf}(t)$, and low $\delta^{18}O$ values (5.75‰–6.38‰), along with radiogenic Sr isotopic signatures, suggest derivation from partial melting of enriched subcontinental lithospheric mantle with contributions from subduction-related components. These rocks formed in association with slab breakoff at ~430 Ma, which created a window for upwelling asthenospheric material and induced the partial melting of subcontinental lithospheric mantle and crust. At ~403 Ma, slab breakoff was nearing its end, leading to weaker asthenospheric upwelling.

Data availability statement

The original contributions presented in the study are included in the article/Supplementary Material, further inquiries can be directed to the corresponding authors.

Author contributions

GC: Data curation, Methodology, Software, Writing–original draft. DL: Data curation, Formal Analysis, Investigation, Software, Supervision, Writing–original draft. XJL: Conceptualization, Methodology, Resources, Software, Supervision, Writing–original draft, Writing–review and editing. PL: Data curation, Formal Analysis, Methodology, Software, Validation, Writing–review and editing. ZB: Data curation, Formal Analysis, Software, Writing–review and editing. XL: Formal Analysis, Methodology, Writing–review and editing. RH: Investigation, Methodology, Writing–review and editing. HT: Data curation, Formal Analysis, Methodology, Writing–review and editing. YL: Formal Analysis, Methodology, Software, Writing–review and editing. WH: Data curation, Formal Analysis, Software, Visualization, Writing–review and editing. YX: Data curation, Formal Analysis, Writing–review and editing.

Funding

The author(s) declare that financial support was received for the research and/or publication of this article. This study was supported financially by funds from the National Natural Science Foundation of China (No. 92055208, 42473063, 42203051), Deep Earth National Science and Technology Key Project (2024ZD1001503) and the Natural Science Foundation of Guangxi Province for Young Scholars (No. GuikeAD23026175, 2022GXNSFBA035538). This research is a contribution to "Xinjiang Tianchi Distinguished Expert" by Xi-Jun Liu.

Conflict of interest

The authors declare that the research was conducted in the absence of any commercial or financial relationships that could be construed as a potential conflict of interest.

Generative AI statement

The author(s) declare that no Generative AI was used in the creation of this manuscript.

Publisher's note

Supplementary material

The Supplementary Material for this article can be found online at: https://www.frontiersin.org/articles/10.3389/feart.2025.1562893/full#supplementary-material

References

Baertschi, P. (1976). Absolute ^{18}O content of standard mean ocean water. *Earth Planet. Sci. Lett.* 31, 341–344. doi:10.1016/0012-821X(76)90115-1

Bird, P. (1979). Continental delamination and the Colorado plateau. *J. Geophys. Res. Solid Earth.* 84 (B13), 7561–7571. doi:10.1029/JB084iB13p07561

Cao, Y., and Song, S. G. (2009). Deformation and metamorphism of HP belt in the North Qilian Mountains and their implications for exhumation. *Acta Petrol Sin.* 25, 2235–2246. (in Chinese with English abstract).

Chen, S., Niu, Y. L., Li, J. Y., Sun, W. L., Zhang, Y., Hu, Y., et al. (2016). Syn-collisional adakitic granodiorites formed by fractional crystallization: insights from their enclosed mafic magmatic enclaves (MMEs) in the Qumushan pluton, North Qilian Orogen at the northern margin of the Tibetan Plateau. *Lithos* 248 (251), 455–468. doi:10.1016/j.lithos.2016.01.033

Chen, Y. X., Song, S. G., Niu, Y. L., and Wei, C. J. (2014). Melting of continental crust during subduction initiation: a case study from the Chaidanuo peraluminous granite in the North Qilian suture zone. *Geochim. Cosmochim. Ac.* 132, 311–336. doi:10.1016/j.gca.2014.02.011

Class, C., Miller, D. M., Goldstein, S. L., and Langmuir, C. H. (2000). Distinguishing melt and fluid subduction components in umnak volcanics, aleutian arc. *Geochem. Geophys. Geosyst.* 1 (6). doi:10.1029/1999GC000010

Defant, M. J., and Drummond, M. S. (1990). Derivation of some modern arc magmas by melting of young subducted lithosphere. *Nature* 347 (6294), 662–665. doi:10.1038/347662a0

Dewey, J. F. (1988). Extensional collapse of orogens. *Tectonics* 7 (6), 1123–1139. doi:10.1029/TC007i006p01123

Dilek, Y., and Furnes, H. (2014). Ophiolites and their origins. *Elements* 10 (2), 93–100. doi:10.2113/gselements.10.2.93

Duan, J., Li, C. S., Qian, Z. Z., and Jiao, J. G. (2015). Geochronological and geochemical constraints on the petrogenesis and tectonic significance of Paleozoic dolerite dykes in the southern margin of Alxa Block, North China Craton. *J. Asian Earth Sci.* 111, 244–253. doi:10.1016/j.jseaes.2015.07.012

Eby, G. N. (1992). Chemical subdivision of the A-type granitoids:Petrogenetic and tectonic implications. *Geology* 20 (7), 641–644. doi:10.1130/0091-7613(1992)020<0641:CSOTAT>2.3.CO;2

Fang, T. H., Wang, C. L., and Wang, R. (1997). Dioritic enclaves and magma mingling in Hexibao granite. *J. Xi'an Coll. Geol.* (04), 53–61. doi:10.19814/j.jese.1997.04.010

Fu, C. L., Yan, Z., Guo, X. Q., Niu, M. L., Cao, B., Wu, Q., et al. (2019). Assembly and dispersal history of continental blocks within the Altun-Qilian-North Qaidam mountain belt, NW China. *Int. Geol. Rev.* 61 (4), 424–447. doi:10.1080/00206814.2018.1428831

Fu, D., Kusky, T. M., Wilde, S. A., Windley, B. F., Polat, A., Huang, B., et al. (2020). Structural anatomy of the early Paleozoic Laohushan ophiolite and subduction complex: implications for accretionary tectonics of the Proto-Tethyan North Qilian orogenic belt, northeastern Tibet. *GSA Bull.* 132 (9–10), 2175–2201. doi:10.1130/B35442.1

Gill, J. B. (1981). "Bulk chemical composition of orogenic andesites," in *Orogenic andesites and plate tectonics*. Editor J. B. Gill (Berlin, Heidelberg: Springer Berlin Heidelberg), 97–167. doi:10.1007/978-3-642-68012-0_5

Gong, J. H., Zhang, J. X., Wang, Z. Q., Yu, S. Y., Li, H. K., and Li, Y. S. (2016). Origin of the Alxa block, western China: new evidence from zircon U–Pb geochronology and Hf isotopes of the longshoushan complex. *Gondwana Res.* 36, 359–375. doi:10.1016/j.gr.2015.06.014

Gong, J. H., Zhang, J. X., and Yu, S. Y. (2013). Redefinition of the Longshoushan Group outcropped in the eastern segment of Longshoushan on the southern margin of Alxa Block:Evidence from detrital zircon U-Pb dating results. *Acta Petrologica Mineralogica* 32 (01), 1–22. (in Chinese with English abstract).

Griffin, W. L., Wang, X., Jackson, S. E., Pearson, N. J., O'Reilly, S. Y., Xu, X., et al. (2002). Zircon chemistry and magma mixing, SE China: in-situ analysis of Hf isotopes, Tonglu and Pingtan igneous complexes. *Lithos* 61 (3), 237–269. doi:10.1016/S0024-4937(02)00082-8

Hart, S. R. (1984). A large-scale isotope anomaly in the Southern Hemisphere mantle. *Nature* 309 (5971), 753–757. doi:10.1038/309753a0

Hawkesworth, C. J., Gallagher, K., Hergt, J. M., and McDermott, F. (1993). Mantle and slab contributions in ARC magmas. *Annu. Rev. Earth Planet. Sci.* 21 (1), 175–204. doi:10.1146/annurev.ea.21.050193.001135

Hawkesworth, C. J., Turner, S. P., McDermott, F., Peate, D. W., and van Calsteren, P. (1997). U-Th isotopes in arc magmas: implications for element transfer from the subducted crust. *Science* 276 (5312), 551–555. doi:10.1126/science.276.5312.551

Hess, P. C. (1992). Phase equilibria constraints on the origin of ocean floor basalts. *Geophys. Monogr. Ser.*, 67–102. doi:10.1029/GM071p0067

Hopkinson, T. N., Harris, N. B. W., Warren, C. J., Spencer, C. J., Roberts, N. M. W., Horstwood, M. S. A., et al. (2017). The identification and significance of pure sediment-derived granites. *Earth Planet. Sci. Lett.* 467, 57–63. doi:10.1016/j.epsl.2017.03.018

Hoskin, P. W. O., and Black, L. P. (2000). Metamorphic zircon formation by solid-state recrystallization of protolith igneous zircon. *J. Metamorph. Geol.* 18 (4), 423–439. doi:10.1046/j.1525-1314.2000.00266.x

Houseman, G. A., McKenzie, D. P., and Molnar, P. (1981). Convective instability of a thickened boundary layer and its relevance for the thermal evolution of continental convergent belts. *J. Geophys. Res.-Solid Earth* 86 (B7), 6115–6132. doi:10.1029/JB086iB07p06115

Huw Davies, J., and von Blanckenburg, F. (1995). Slab breakoff: a model of lithosphere detachment and its test in the magmatism and deformation of collisional orogens. *Earth Planet. Sci. Lett.* 129 (1), 85–102. doi:10.1016/0012-821X(94)00237-S

Jahn, B. M., Wu, F. Y., Lo, C. H., and Tsai, C. H. (1999). Crust–mantle interaction induced by deep subduction of the continental crust: geochemical and Sr–Nd isotopic evidence from post-collisional mafic–ultramafic intrusions of the northern Dabie complex, central China. *Chem. Geol.* 157 (1), 119–146. doi:10.1016/S0009-2541(98)00197-1

Johnson, M. C., and Plank, T. (2000). Dehydration and melting experiments constrain the fate of subducted sediments. *Geochem. Geophys. Geosyst.* 1 (12). doi:10.1029/1999GC000014

Kang, H., Chen, Y. L., Li, D. P., Bao, C., and Zhang, H. Z. (2018). Zircon U-Pb ages and Hf isotopic compositions of fluvial sediments from the Huangshui, Beichuan, and Xichuan rivers, Northwest China: constraints on the formation and evolution history of the Central Qilian Block. *Geochem. J.* 52 (1), 37–57. doi:10.2343/geochemj.2.0495

Kay, R. W., and Mahlburg Kay, S. (1993). Delamination and delamination magmatism. *Tectonophysics* 219 (1), 177–189. doi:10.1016/0040-1951(93)90295-U

Li, X. H., Li, W. X., Wang, X. C., Li, Q. L., Liu, Y., and Tang, G. Q. (2009). Role of mantle-derived magma in genesis of early Yanshanian granites in the Nanling Range, South China: *in situ* zircon Hf-O isotopic constraints. *Sci. China, D. Earth Sci.* 52 (9), 1262–1278. doi:10.1007/s11430-009-0117-9

Li, X. H., Long, W. G., Li, Q. L., Liu, Y., Zheng, Y. F., Yang, Y. H., et al. (2010). Penglai zircon megacrysts: a potential new working reference material for microbeam determination of Hf–O isotopes and U–Pb age. *Geostand. Geoanal. Res.* 34, 117–134. doi:10.1111/j.1751-908X.2010.00036.x

Li, X. H., Su, L., Chung, S. L., Li, Z. X., Liu, Y., Song, B., et al. (2005). Formation of the Jinchuan ultramafic intrusion and the world's third largest Ni-Cu sulfide deposit: associated with the ~825 Ma south China mantle plume? *Geochem Geophys Geosyst* 6 (11). doi:10.1029/2005GC001006

Li, X. H., Tang, G. Q., Gong, B., Yang, Y. H., Hou, K. J., Hu, Z. C., et al. (2013). Qinghu zircon: a working reference for microbeam analysis of U-Pb age and Hf and O isotopes. *Chin. Sci. Bull.* 58, 4647–4654. doi:10.1007/s11434-013-5932-x

Liégeois, J. P. (1998). Preface–Some words on the post-collisional magmatism. *Lithos* 45, XV–XVIII. doi:10.1130/0-8137-2409-0.v

Liu, J. N., Yin, C. Q., Zhang, J., Qian, J. H., Li, S., Xu, K. Y., et al. (2020). Tectonic evolution of the Alxa Block and its affinity: evidence from the U-Pb geochronology and Lu-Hf isotopes of detrital zircons from the Longshoushan Belt. *Precambrian Res.* 344, 105733. doi:10.1016/j.precamres.2020.105733

Liu, P. D., Liu, X. J., Xiao, W. J., Zhang, Z. G., Song, Y. J., Xiao, Y., et al. (2021). Geochronology, geochemistry, and Sr-Nd isotopes of Early Carboniferous magmatism in southern West Junggar, northwestern China: implications for Junggar oceanic plate subduction. *J. Arid. Land* 13, 1163–1182. doi:10.1007/s40333-021-0069-2

Liu, P. D., Liu, X. J., Xiao, W. J., Zhang, Z. G., Xiao, Y., Song, Y. J., et al. (2023). Multiple ridge subduction processes in the southern Altaids: implications from clinopyroxene chemistry and Sr–Nd–Hf isotopes of late carboniferous Nb-enriched, magnesian diorite-andesites in West Junggar, NW China. *Chem. Geol.* 635, 121600. doi:10.1016/j.chemgeo.2023.121600

Liu, Q., Zhao, G. C., Sun, M., Han, Y. G., Eizenhöfer, P. R., Hou, W. Z., et al. (2016). Early paleozoic subduction processes of the paleo-asian ocean: insights from geochronology and geochemistry of paleozoic plutons in the Alxa terrane. *Lithos* 262, 546–560. doi:10.1016/j.lithos.2016.07.041

Liu, W. H., Liu, X. D., Pan, J. Y., Wang, K. X., Wang, G., Niu, Y. B., et al. (2019). Magma mixing genesis of the mafic enclaves in the Qingshanbao complex of longshou mountain, China: evidence from petrology, geochemistry, and zircon chronology. *Minerals* 9, 195. doi:10.3390/min9030195

Liu, X. J., Xu, J. F., Castillo, P. R., Xiao, W. J., Shi, Y., Feng, Z. H., et al. (2014). The Dupal isotopic anomaly in the southern Paleo-Asian Ocean: Nd–Pb isotope evidence from ophiolites in Northwest China. *Lithos* 189 (0), 185–200. doi:10.1016/j.lithos.2013.08.020

Liu, X. J., Xu, J. F., Castillo, P. R., Xiao, W. J., Shi, Y., Zhang, Z. G., et al. (2021b). Long-lived low Th/U Pacific-type isotopic mantle domain: constraints from Nd and Pb isotopes of the Paleo-Asian Ocean mantle. *Earth Planet. Sci. Lett.* 567, 117006. doi:10.1016/j.epsl.2021.117006

Liu, Y. S., Hu, Z. C., Gao, S., Günther, D., Xu, J., Gao, C. G., et al. (2008). *In situ* analysis of major and trace elements of anhydrous minerals by LA-ICP-MS without applying an internal standard. *Chem. Geol.* 257 (1), 34–43. doi:10.1016/j.chemgeo.2008.08.004

Ludwig, K. R. (2003). User's manual for a geochronological toolkit for Microsoft Excel (Isoplot/Ex version 3.0). *Spec. Publ.* 4 (4), 1–71.

Maitre, R. W. L., Streckeisen, A., Zanettin, B., and Rocks, I. S. o.t.S. o.I. (1986). A chemical classification of volcanic rocks based on the total alkali-silica diagram. *J. Petrol.* 27 (3), 745–750. doi:10.1093/petrology/27.3.745

Mazza, S. E., Stracke, A., Gill, J. B., Kimura, J.-I., and Kleine, T. (2020). Tracing dehydration and melting of the subducted slab with tungsten isotopes in arc lavas. *Earth Planet. Sci. Lett.* 530, 115942. doi:10.1016/j.epsl.2019.115942

Molnar, P., Houseman, G. A., and Conrad, C. P. (1998). Rayleigh—taylor instability and convective thinning of mechanically thickened lithosphere: effects of non-linear viscosity decreasing exponentially with depth and of horizontal shortening of the layer. *Geophys. J. Int.* 133 (3), 568–584. doi:10.1046/j.1365-246X.1998.00510.x

Nowell, G. M., Kempton, P. D., Noble, S. R., Fitton, J. G., Saunders, A. D., Mahoney, J. J., et al. (1998). High precision Hf isotope measurements of MORB and OIB by thermal ionisation mass spectrometry: insights into the depleted mantle. *Chem. Geol.* 149 (3), 211–233. doi:10.1016/S0009-2541(98)00036-9

Pearce, J. (1996). Sources and settings of granitic rocks. *Int. Union Geol. Sci.* 19 (4), 120–125. doi:10.18814/epiiugs/1996/v19i4/005

Pearce, J., and Peate, D. (1995). Tectonic implications of the composition of volcanic ARC magmas. *Annu. Rev. Earth Planet. Sci.* 23, 251–285. doi:10.1146/annurev.ea.23.050195.001343

Pearce, J. A. (2008). Geochemical fingerprinting of oceanic basalts with applications to ophiolite classification and the search for Archean oceanic crust. *Lithos* 100 (1), 14–48. doi:10.1016/j.lithos.2007.06.016

Pearce, J. A., and Parkinson, I. J. (1993). Trace element models for mantle melting: application to volcanic arc petrogenesis. *Geol. Soc. Spec. Publ.* 76 (1), 373–403. doi:10.1144/GSL.SP.1993.076.01.19

Pearce, N. J. G., Westgate, J. A., Gatti, E., Pattan, J. N., Parthiban, G., and Achyuthan, H. (2014). Individual glass shard trace element analyses confirm that all known Toba tephra reported from India is from the c. 75-ka Youngest Toba eruption. *J. Quat. Sci.* 29 (8), 729–734. doi:10.1002/jqs.2741

Plank, T., and Langmuir, C. H. (1998). The chemical composition of subducting sediment and its consequences for the crust and mantle. *Chem. Geol.* 145 (3), 325–394. doi:10.1016/S0009-2541(97)00150-2

Qian, Q., Zhang, Q., Sun, X. M., and Wang, Y. M. (2001). Geochemical features and tectonic setting for basalts and cherts from Laohushan, North Qilian. *Chin. J. Geol.* (04), 444–453. (in Chinese with English abstract).

Rudnick, R. L., and Gao, S. (2003). "3.01-Composition of the continental crust," in *Treatise on geochemistry*. Editors H. D. Holland, and K. K. Turekian (Oxford: Pergamon), 1–64.

Saunders, A. D., Storey, M., Kent, R. W., and Norry, M. J. (1992). Consequences of plume-lithosphere interactions. *Geol. Soc. Spec. Publ.* 68 (1), 41–60. doi:10.1144/GSL.SP.1992.068.01.04

Song, S. G., Niu, Y. L., Su, L., and Xia, X. H. (2013). Tectonics of the North qilian orogen, NW China. *Gondwana Res.* 23 (4), 1378–1401. doi:10.1016/j.gr.2012.02.004

Song, S. G., Niu, Y. L., Su, L., Zhang, C., and Zhang, L. F. (2014). Continental orogenesis from ocean subduction, continent collision/subduction, to orogen collapse, and orogen recycling: the example of the North Qaidam UHPM belt, NW China. *Earth-Sci. Rev.* 129, 59–84. doi:10.1016/j.earscirev.2013.11.010

Song, S. G., Yang, L. M., Zhang, Y. Q., Niu, Y. L., Wang, C., Su, L., et al. (2017). Qi-Qin Accretionary Belt in Central China Orogen: accretion by trench jam of oceanic plateau and formation of intra-oceanic arc in the Early Paleozoic Qin-Qi-Kun Ocean. *Sci. Bull.* 62 (15), 1035–1038. doi:10.1016/j.scib.2017.07.009

Song, S. G., Zhang, L. F., Niu, Y., Wei, C. J., Liou, J. G., and Shu, G. M. (2007). Eclogite and carpholite-bearing metasedimentary rocks in the North Qilian suture zone, NW China: implications for Early Palaeozoic cold oceanic subduction and water transport into mantle. *J. Metamorph. Geol.* 25 (5), 547–563. doi:10.1111/j.1525-1314.2007.00713.x

Sun, W. D., and McDonough, W. (1989). Chemical and isotopic systematics of oceanic basalts: implications for mantle composition and processes. *Geol. Soc. Lond. Spec. Publ.* 42 (1), 313–345. doi:10.1144/GSL.SP.1989.042.01.19

Tatsumi, Y., and Takahashi, T. (2006). Operation of subduction factory and production of andesite. *J. Mineral. Petrol. Sci.* 101 (3), 145–153. doi:10.2465/jmps.101.145

Thompson, P. M. E., Kempton, P. D., and Kerr, A. C. (2008). Evaluation of the effects of alteration and leaching on Sm–Nd and Lu–Hf systematics in submarine mafic rocks. *Lithos* 104 (1), 164–176. doi:10.1016/j.lithos.2007.12.005

Tseng, C. Y., Yang, H. J., Yang, H. Y., Liu, D., Wu, C., Cheng, C. K., et al. (2009). Continuity of the North qilian and North qinling orogenic belts, central orogenic system of China: evidence from newly discovered paleozoic adakitic rocks. *Gondwana Res.* 16 (2), 285–293. doi:10.1016/j.gr.2009.04.003

Valley, J. W., Kinny, P. D., Schulze, D. J., and Spicuzza, M. J. (1998). Zircon megacrysts from kimberlite: oxygen isotope variability among mantle melts. *Contrib. Mineral. Petrol.* 133 (1), 1–11. doi:10.1007/s004100050432

Vanderhaeghe, O., and Teyssier, C. (2001). Crustal-scale rheological transitions during late-orogenic collapse. *Tectonophysics* 335 (1), 211–228. doi:10.1016/S0040-1951(01)00053-1

van Hunen, J., and Miller, M. S. (2015). Collisional processes and links to episodic changes in subduction zones. *Elements* 11 (2), 119–124. doi:10.2113/gselements.11.2.119

Vervoort, J. D., and Blichert-Toft, J. (1999). Evolution of the depleted mantle: Hf isotope evidence from juvenile rocks through time. *Geochim. Cosmochim. Acta* 63 (3), 533–556. doi:10.1016/S0016-7037(98)00274-9

Vervoort, J. D., Plank, T., and Prytulak, J. (2011). The Hf–Nd isotopic composition of marine sediments. *Geochim. Cosmochim. Acta* 75 (20), 5903–5926. doi:10.1016/j.gca.2011.07.046

von Blanckenburg, F., and Davies, J. H. (1995). Slab breakoff: a model for syncollisional magmatism and tectonics in the Alps. *Tectonics* 14 (1), 120–131. doi:10.1029/94tc02051

Wang, C. Y., Zhang, Q., Qian, Q., and Zhou, M. F. (2005). Geochemistry of the early paleozoic baiyin volcanic rocks (NW China): implications for the tectonic evolution of the North qilian orogenic belt. *J. Geol.* 113 (1), 83–94. doi:10.1086/425970

Wang, K. X., Yu, C. D., Yan, J., Liu, X. D., Liu, W. H., and Pan, J. Y. (2019). Petrogenesis of early silurian granitoids in the longshoushan area and their implications for the extensional environment of the North qilian orogenic belt, China. *Lithos* 342–343, 152–174. doi:10.1016/j.lithos.2019.05.029

Wei, C. J., and Song, S. G. (2008). Chloritoid–glaucophane schist in the north Qilian orogen, NW China: phase equilibria and P–T path from garnet zonation. *J. Metamorph. Geol.* 26 (3), 301–316. doi:10.1111/j.1525-1314.2007.00753.x

Wei, C. J., Yang, Y., Su, X. L., Song, S. G., and Zhang, L. F. (2009). Metamorphic evolution of low-T eclogite from the North Qilian orogen, NW China: evidence from petrology and calculated phase equilibria in the system NCKFMASHO. *J. Metamorph. Geol.* 27 (1), 55–70. doi:10.1111/j.1525-1314.2008.00803.x

Workman, R. K., and Hart, S. R. (2005). Major and trace element composition of the depleted MORB mantle (DMM). *Earth Planet. Sci. Lett.* 231 (1), 53–72. doi:10.1016/j.epsl.2004.12.005

Wu, C., Zuza, A. V., Yin, A., Chen, X. H., Haproff, P. J., Li, J., et al. (2021). Punctuated orogeny during the assembly of asia: tectonostratigraphic evolution of the North China Craton and the qilian Shan from the paleoproterozoic to early paleozoic. *Tectonics* 40 (4), e2020TC006503. doi:10.1029/2020TC006503

Wu, C. L., Gao, Y., Frost, B. R., Robinson, P. T., Wooden, J. L., Wu, S., et al. (2011). An early Palaeozoic double-subduction model for the North Qilian oceanic plate: evidence from zircon SHRIMP dating of granites. *Int. Geol. Rev.* 53 (2), 157–181. doi:10.1080/00206810902965346

Wu, C. L., Xu, X. Y., Gao, Q. M., Li, X. M., Lei, M., Gao, Y. H., et al. (2010). Early palaezoic grranitoid magmatism and tectonic evolution in north oilian, NW China. Acta petrol. *Sin.* 26 (04), 1027–1044. (in Chinese with English abstract).

Wu, C. L., Yang, J. S., Yi, Y. H., L.Wooden, J., Shi, R. D., Chen, S. Y., et al. (2004). Dating of two types of granite from north Qilian,China. *Acta Petrol. Sin. (03)*, 425–432. (in Chinese with English abstract).

Wu, F. Y., Walker, R. J., Yang, Y. H., Yuan, H. L., and Yang, J. H. (2006). The chemical-temporal evolution of lithospheric mantle underlying the North China Craton. *Geochim. Cosmochim. Acta* 70 (19), 5013–5034. doi:10.1016/j.gca.2006.07.014

Wu, H. Q., Feng, Y. M., and Song, S. G. (1993). Metamorphism and deformation of blueschist belts and their tectonic implications, North Qilian Mountains, China. *J. Metamorph. Geol.* 11 (4), 523–536. doi:10.1111/j.1525-1314.1993.tb00169.x

Xia, L. Q., Xia, Z. C., and Xu, X. Y. (2003). Magmagenesis in the ordovician backarc basins of the northern qilian mountains, China. *GSA Bull.* 115 (12), 1510–1522. doi:10.1130/B25269.1

Xia, X. H., Song, S. G., and Niu, Y. L. (2012). Tholeiite–Boninite terrane in the North Qilian suture zone: implications for subduction initiation and back-arc basin development. *Chem. Geol.* 328, 259–277. doi:10.1016/j.chemgeo.2011.12.001

Xu, Y. J., Du, Y. S., Cawood, P. A., Guo, H., Huang, H., and An, Z. H. (2010). Detrital zircon record of continental collision: assembly of the Qilian Orogen, China. *Sediment. Geol.* 230 (1), 35–45. doi:10.1016/j.sedgeo.2010.06.020

Xue, S., Ling, M. X., Liu, Y. L., Zhang, H., and Sun, W. D. (2017). The genesis of early Carboniferous adakitic rocks at the southern margin of the Alxa Block, North China. *Lithos* 278–281, 181–194. doi:10.1016/j.lithos.2017.01.012

Yang, Q., Xia, X. P., Zhang, W. F., Zhang, Y. Q., Xiong, B. Q., Xu, Y. G., et al. (2018). An evaluation of precision and accuracy of SIMS oxygen isotope analysis. *Solid Earth Sci.* 3, 81–86. doi:10.1016/j.sesci.2018.05.001

Yang, X. Q., Zhang, Z. H., Jiang, Z. S., and Duan, S. G. (2018). Geochronology, petrogenesis and tectonic significance of Huashugou granitoids in North Qilian, NW China. *Lithos* 314–315, 497–505. doi:10.1016/j.lithos.2018.06.023

Yang, Y. H., Wu, F. Y., Wilde, S. A., Liu, X. M., Zhang, Y. B., Xie, L. W., et al. (2009). *In situ* perovskite Sr–Nd isotopic constraints on the petrogenesis of the Ordovician Mengyin kimberlites in the North China Craton. *Chem. Geol.* 264 (1), 24–42. doi:10.1016/j.chemgeo.2009.02.011

Yu, S. Y., Zhang, J. X., Qin, H. P., Sun, D. Y., Zhao, X. L., Cong, F., et al. (2015). Petrogenesis of the early Paleozoic low-Mg and high-Mg adakitic rocks in the North Qilian orogenic belt, NW China: implications for transition from crustal thickening to extension thinning. *J. Asian Earth Sci.* 107, 122–139. doi:10.1016/j.jseaes.2015.04.018

Zeng, R. Y., Lai, J. Q., Mao, X. C., Li, B., Ju, P. J., and Tao, S. L. (2016). Geochemistry, zircon U–Pb dating and Hf isotopies composition of Paleozoic granitoids in Jinchuan, NW China: constraints on their petrogenesis, source characteristics and tectonic implication. *J. Asian Earth Sci.* 121, 20–33. doi:10.1016/j.jseaes.2016.02.009

Zhang, J. R., Wei, C. J., and Chu, H. (2018). New model for the tectonic evolution of Xing' an-Inner Mongolia Orogenic Belt: evidence from four different phases of metamorphism in Central Inner Mongolia. *Acta Petrol. Sin.* 34, 2857–2872. (in Chinese with English abstract).

Zhang, J. X., Yu, S. Y., and Mattinson, C. G. (2017a). Early Paleozoic polyphase metamorphism in northern Tibet, China. *Gondwana Res.* 41, 267–289. doi:10.1016/j.gr.2015.11.009

Zhang, L. Q., Zhang, H. F., Hawkesworth, C., Luo, B. J., and Yang, H. (2021a). Mafic rocks from the southern Alxa block of Northwest China and its geodynamic evolution in the Paleozoic. *J. Geol. Soc.* 178 (3), jgs2020–038. doi:10.1144/jgs2020-038

Zhang, L. Q., Zhang, H. F., Hawkesworth, C., Luo, B. J., Yang, H., Xu, W. C., et al. (2019). Sediment contribution in post-collisional high Ba-Sr magmatism: evidence from the Xijing pluton in the Alxa block, NW China. *Gondwana Res.* 69, 177–192. doi:10.1016/j.gr.2018.12.010

Zhang, L. Q., Zhang, H. F., Zhang, S. S., Xiong, Z. L., Luo, B. J., Yang, H., et al. (2017b). Lithospheric delamination in post-collisional setting: evidence from intrusive magmatism from the North Qilian orogen to southern margin of the Alxa block, NW China. *Lithos* 288–289, 20–34. doi:10.1016/j.lithos.2017.07.009

Zhang, Y. S., Zhang, Y. M., Gu, X. X., Wang, J. L., Yao, B., and Sui, H. P. (2023). Two-stage crust-mantle interactions from oceanic subduction to post-collisional extension in the northern margin of the North China Craton: insights from Paleozoic to Mesozoic magmatism. *GSA Bull.* 136, 2767–2788. doi:10.1130/B37209.1

Zhang, Z. G., Liu, X. J., Xiao, W. J., Xu, J. F., Shi, Y., Gong, X. H., et al. (2021b). Geochemistry and Sr–Nd–Hf–Pb isotope systematics of late Carboniferous sanukitoids in northern West Junggar, NW China: implications for initiation of ridge-subduction. *Gondwana Res.* 99, 204–218. doi:10.1016/j.gr.2021.07.008

Zhao, X. C., Liu, C. Y., Wang, J. Q., Zhao, Y., Wang, L., and Zhang, Q. H. (2016). Detrital zircon U–Pb ages of Paleozoic sedimentary rocks from the eastern Hexi Corridor Belt (NW China): provenance and geodynamic implications. *Sediment. Geol.* 339, 32–45. doi:10.1016/j.sedgeo.2016.04.005

Zhou, X. C., Zhang, H. F., Luo, B. J., Pan, F. B., Zhang, S. S., and Guo, L. (2016). Origin of high Sr/Y-type granitic magmatism in the southwestern of the Alxa Block, Northwest China. *Lithos* 256–257, 211–227. doi:10.1016/j.lithos.2016.04.021

Zindler, A., and Hart, S. (1986). Chemical geodynamics. *Annu. Rev. Earth Planet. Sci.* 14 (1), 493–571. doi:10.1146/annurev.ea.14.050186.002425